Master's Thesis

Homogeneous RF Field Distribution Optimization in 3T Abdominal Imaging

Paul de Heer

Supervisors:
prof. dr. Andrew Webb*
dr. ir. Bert Jan Kooij†
dr. ir. Rob Remis†

January 21, 2013

* C.J. Gorter Center for High Field MRI, Department of Radiology, University Medical Center, Leiden, The Netherlands.

† Telecommunications Department, Delft University of Technology, Delft, The Netherlands.

Abstract

The appearance of severe signal drop-outs in abdominal Magnetic Resonance Imaging at 3 Tesla arises primarily from areas of very low magnetic flux density $\mathbf{B}_1$ of the transmit field in the body, and is problematic in both obese as well as very thin subjects. In this study, we show how thin patient-friendly pads containing new high permittivity materials can be designed and optimized, and when placed around the subject increase substantially the $\mathbf{B}_1$ uniformity and the image quality. Results from nine healthy volunteers show that inclusion of these dielectric pads results in statistically significant decreases in the coefficient of variance of the $\mathbf{B}_1$ field, with stronger and more uniform fields being produced. In addition there are statistically significant decreases in time-averaged power required for scanning. These differences are present in both quadrature-mode operation (coefficient of variance decrease, $P < 0.0001$, mean $25.4 \pm 10\%$: power decrease, $P = 0.005$, mean $14 \pm 14\%$) and also for the RF-shimmed case (coefficient of variance decrease, $P = 0.01$, mean $16 \pm 13\%$: power decrease, $P = 0.005$, mean $22 \pm 11\%$) of a dual-transmit system.

Acknowledgements

I like to thank the LUMC for giving me the opportunity to work on this research. Also I would like to thank Bert Jan Kooij and Rob Remis who guided me during my thesis and gave great support on the theoretical side of the thesis. I especially want to thank Andrew Webb who's advice and support have kept me on track. I also want to express my gratitude to Wyger Brink and Joep Wezel for their help. Furthermore, I would like to thank all the people at the Gorter Center for their help and for making me feel at home in Leiden. Finally, I would like to thank my friends and family for their support.

Paul de Heer
Leiden, The Netherlands
January 21, 2013

Preface

This master thesis is the conclusion of my master program Electrical Engineering at Delft University of Technology. This work also concludes my intern ship at the Gorter Centre of Leiden University Medical Center (LUMC).

When I heard about a possible master thesis subject at the LUMC it was something that really sparked my interest. I think the medical environment with its many technical challenges is inspiring and gives the satisfaction to keep on researching. I have had a great time doing the research and had several high points like presenting the work at the ISMRM Benelux conference in Belgium.

If you would ask me before I started my thesis if I would do a PhD after my graduation the answer would probably be no. But after doing my thesis research, which I enjoyed so much, I am happy to say that after my graduation I will continue as a PhD student at the LUMC.

Contents

Chapter 1

Introduction

1.1 Problem statement

The appearance of so-called signal voids in abdominal MRI at 3 tesla (3 T) has been noted by many researchers [1, 2, 3, 4, 5, 6] and is one of the reasons why a large part of clinical MRI is almost always still studied at 1.5 T [5, 6]. Signals voids are the result of a spatially varying B_1^+ field. To obtain MRI images with an even contrast and minimal signals voids, the B_1^+ field should be as homogeneous as possible. However, for MRI scanners operating at 3 tesla and above, solving this problem is far from trivial. As pointed out by Bernstein [1] "Image shading and uneven contrast resulting from spatial variation in the transmit B_1^+ field remains one of the biggest unsolved problems for routine clinical 3 T imaging today."

The clinical, and implicitly financial, importance of this situation is emphasized by the recent commercial introduction of dual-transmit RF systems at 3 T, in which the quadrature body coil is effectively split into two linear coils, each of which can be driven with an independently controlled magnitude and phase. The two degrees of freedom (relative amplitudes and relative phases of the two channels) compared to only one (absolute amplitude) for a conventional single transmit system can produce considerable increases in RF transmit homogeneity [7, 8], as has long been known theoretically and investigated extensively for imaging at 7 T [9, 10]. However, experiments carried out at the Gorter Centre of the LUMC and elsewhere indicates that, despite improved performance, dual-channel 3 T systems do not consistently solve the problem of image inhomogeneities. Experimental and simulation

work has suggested that there are still further improvements using an eight channel transmit body coil [11, 12], but such a setup is not currently commercially available. The dual transmit solution is not available for all hospitals because of the high costs of such a system which are estimated to be about 1 million dollar. A second approach to address the issues of RF inhomogeneity in 3 T abdominal imaging is the use of "dielectric pads" [13, 14, 15, 16]. Typically these pads are made from ultrasound gel with dissolved paramagnetics such as manganese chloride to give a short T_2 and hence low background MR signal. There are several problems with this approach as currently implemented. From a practical point-of-view the pad is 3-cm thick and therefore somewhat patient-unfriendly. In the usual implementation, a single pad is placed centrally on top of the patient irrespective of the patient size: the large thickness makes it impractical to place a second one underneath the patient to improve the transmit field in the posterior regions. Perhaps most importantly, presently it is not clear how to optimize a pad (by changing its size, shape, thickness, placement, or relative permittivity) in a systematic way.

1.2 Project goal

In this report, we study the effects of various pad properties on the homogeneity of the B_1^+ field. The shape, the placement, its conductivity and the permittivity of a pad are all considered. Furthermore, we present both electromagnetic (EM) simulations and experimental (in-vivo) data using thin pads with high permittivity materials based upon aqueous suspensions of metal titanates [17, 18] which have a relative permittivity of 300. The imaging performance both with and without dielectric pads is compared experimentally to that of a dual-channel RF system in quadrature mode, as well as the combined approach using both the dielectric pads and RF shimming.

1.3 Thesis outline

The outline of this thesis is as follows:

Chapter 2: Basic electromagnetic equations

In Chapter 2, we present the basic equations that govern electromagnetic wave phenomena. From the local form of Maxwell's equations we derive a pair of coupled integral equations from which the field in inhomogeneous media can be evaluated.

Chapter 3: Basics Magnetic Resonance Imaging

Chapter 3 gives a brief overview of Magnetic Resonance Imaging. The parts of an MRI scanner are described and the basic physical principles of MRI are discussed as well.

Chapter 4: Simplified pad model

In Chapter 4 we study the effects of the shape and conductvity of the pads on the homogeneity of the B_1^+ field. The field patterns produced by high permittivity pads are studied as well.

Chapter 5: Numerical simulations and results

Chapter 5 describes how the pads have been optimized in size, placement and material properties for realistic male and female models using the FDTD method.

Chapter 6: In-Vivo results

Chapter 6 shows the in-vivo results of the MRI scans with and without pads and gives a statistical analysis of these results.

Chapter 7: Discussion and conclusion

The conclusions and recommendations are presented in Chapter 7.

Chapter 2

Basic electromagnetic equations

2.1 Time domain Maxwell's equations

To describe the behaviour of electromagnetic waves in vacuum we can use the macroscopic version of Maxwell's equations. In vector notation, these equations are given by

$$-\boldsymbol{\nabla} \times \mathbf{H} + \varepsilon_0 \partial_t \mathbf{E} = -\mathbf{J}^{\mathrm{mat}}, \tag{2.1.1}$$

$$\boldsymbol{\nabla} \times \mathbf{E} + \mu_0 \partial_t \mathbf{H} = -\mathbf{K}^{\mathrm{mat}}, \tag{2.1.2}$$

where $\mathbf{E}$ (V/m) is the electric field strength, $\mathbf{H}$ (A/m) is the magnetic field strength, and the permittivity and permeability of vacuum are given by ε_0 and μ_0, respectively. Furthermore, $\mathbf{J}^{\mathrm{mat}}$ is the volume density of electric current ($\mathrm{A/m^2}$) and the volume density of magnetic current is given by $\mathbf{K}^{\mathrm{mat}}$ ($\mathrm{V/m^2}$). The latter two quantities take the presence of matter into account and vanish in a vacuum domain. Writing these currents as a superposition of induced and external currents, we have

$$\mathbf{J}^{\mathrm{mat}} = \mathbf{J}^{\mathrm{ind}} + \mathbf{J}^{\mathrm{ext}} \tag{2.1.3}$$

and

$$\mathbf{K}^{\mathrm{mat}} = \mathbf{K}^{\mathrm{ind}} + \mathbf{K}^{\mathrm{ext}}, \tag{2.1.4}$$

where $\mathbf{J}^{\mathrm{ind}}$ and $\mathbf{K}^{\mathrm{ind}}$ are the induced field-dependent current densities, while $\mathbf{J}^{\mathrm{ext}}$ and $\mathbf{K}^{\mathrm{ext}}$ are the external field-independent current densities. The external currents describe the action of the sources that generate the electromagnetic field. The induced currents describe the reaction of matter to the

presence of an electromagnetic field. To describe this reaction, it is customary to write the induced currents as

$$\mathbf{J}^{\text{ind}} = \mathbf{J} + \partial_t \mathbf{P} \tag{2.1.5}$$

and

$$\mathbf{K}^{\text{ind}} = \mu_0 \partial_t \mathbf{M}, \tag{2.1.6}$$

where $\mathbf{J}$ is the conduction current (A/m^2), $\mathbf{P}$ is the electric polarization (C/m^2), and $\mathbf{M}$ is the magnetization (A/m). For most materials, we have $\mathbf{J} = \mathbf{J}(\mathbf{E})$, $\mathbf{P} = \mathbf{P}(\mathbf{E})$, and $\mathbf{M} = \mathbf{M}(\mathbf{H})$, that is, the conduction current and polarization depend only on the electric field strength, while the magnetization depends only on the magnetic field strength.

With the introduction of all these field quantities, Maxwell's equations become

$$-\boldsymbol{\nabla} \times \mathbf{H} + \partial_t \big(\varepsilon_0 \mathbf{E} + \mathbf{P}\big) + \mathbf{J} = -\mathbf{J}^{\text{ext}}, \tag{2.1.7}$$

$$\boldsymbol{\nabla} \times \mathbf{E} + \partial_t \mu_0 \big(\mathbf{H} + \mathbf{M}\big) = -\mathbf{K}^{\text{ext}}. \tag{2.1.8}$$

Finally, introducing the electric flux density $\mathbf{D}$ (C/m^2) and the magnetic flux density $\mathbf{B}$ (T) as

$$\mathbf{D} = \varepsilon_0 \mathbf{E} + \mathbf{P} \tag{2.1.9}$$

and

$$\mathbf{B} = \mu_0 \big(\mathbf{H} + \mathbf{M}\big), \tag{2.1.10}$$

we arrive at

$$-\boldsymbol{\nabla} \times \mathbf{H} + \partial_t \mathbf{D} + \mathbf{J} = -\mathbf{J}^{\text{ext}}, \tag{2.1.11}$$

$$\boldsymbol{\nabla} \times \mathbf{E} + \partial_t \mathbf{B} = -\mathbf{K}^{\text{ext}}. \tag{2.1.12}$$

The SI units of all the field quantities that we have introduced are summarized in Table 2.1.

Symbol	Unit	Quantity
$\mathbf{E}$	V/m	electric field strength
$\mathbf{H}$	A/m	magnetic field strength
$\mathbf{D}$	$\mathrm{C/m^2}$	electric flux density
$\mathbf{B}$	T	magnetic flux density
$\mathbf{J}$	$\mathrm{A/m^2}$	electric current density
$\mathbf{K}$	$\mathrm{V/m^2}$	magnetic current density
$\mathbf{P}$	$\mathrm{C/m^2}$	electric polarization
$\mathbf{M}$	A/m	magnetization
σ	S/m	conductivity
ε	F/m	permittivity
μ	H/m	permeability

Table 2.1: Electromagnetic field quantities and their SI-units

2.1.1 Compatibility relations

Supplementary relations are obtained when we apply the divergence operator $(\boldsymbol{\nabla}\cdot)$ to Eqs. (2.1.11) and (2.1.12). This yields the time domain compatibility relations

$$\partial_t \boldsymbol{\nabla}\cdot\mathbf{D} + \boldsymbol{\nabla}\cdot\mathbf{J} = -\boldsymbol{\nabla}\cdot\mathbf{J}^{\mathrm{ext}} \tag{2.1.13}$$

and

$$\partial_t \boldsymbol{\nabla}\cdot\mathbf{B} = -\boldsymbol{\nabla}\cdot\mathbf{K}^{\mathrm{ext}}. \tag{2.1.14}$$

Eq. (2.1.13) expresses conservation of charge and with $\mathbf{K}^{\mathrm{ext}} = \mathbf{0}$ it follows from Eq. (2.1.14) that the magnetic flux density is divergence-free.

2.1.2 Constitutive relations

The constitutive relations describe the macroscopic reaction of matter to an electromagnetic field and relate the electric conduction current and the electric and magnetic flux densities to the fields. In this report, we restrict ourselves to media with constitutive relations

$$\mathbf{J} = \sigma\mathbf{E} \quad \text{and} \quad \mathbf{D} = \varepsilon\mathbf{E}, \tag{2.1.15}$$

where σ is the conductivity of the material (S/m) and ε is the permittivity (F/m). For common materials (tissue) placed in an MRI scanner, the constitutive relation connecting the magnetization $\mathbf{M}$ to the magnetic flux density $\mathbf{B}$ is not so simple as the constitutive relations given above. Specifically, the connection between $\mathbf{B}$ and $\mathbf{M}$ is given by the Bloch equations [19]. In their most simple form (neglecting relaxation effects), these equations are given by

$$\partial_t \mathbf{M} = \gamma(\mathbf{M} \times \mathbf{B}),$$

where γ is the so-called gyromagnetic ratio ($\mathrm{rad\,s^{-1}\,T^{-1}}$). The fundamentals of MRI can be classically explained using the Bloch equations and a brief overview is presented in Chapter 3. In vacuum, however, the constitutive relation is very simple and is given by

$$\mathbf{B} = \mu_0 \mathbf{H}. \tag{2.1.16}$$

The medium parameters that we have introduced are summarized in Table 2.1.

2.1.3 The boundary conditions

Across the interfaces where the constitutive parameters show a jump discontinuity, the tangential components of the electric and magnetic field strengths are to be continuous. To be more precise, let $\mathcal{S}$ denote a source-free and time-invariant interface and assume that $\mathcal{S}$ has everywhere a unique tangent plane. Further, let $\boldsymbol{n}$ denote the unit vector along the normal to $\mathcal{S}$ such that upon traversing $\mathcal{S}$ in the direction of $\boldsymbol{n}$, we pass from the domain $\mathcal{D}_2$ to the domain $\mathcal{D}_1$, $\mathcal{D}_1$ and $\mathcal{D}_2$ being located at either side of $\mathcal{S}$ (see Fig. 1).Then at the boundary $\mathcal{S}$ we have the following boundary conditions:

$$\boldsymbol{n} \times \boldsymbol{E} \quad \text{is continuous across } \mathcal{S}, \tag{2.1.17}$$

and

$$\boldsymbol{n} \times \boldsymbol{H} \quad \text{is continuous across } \mathcal{S}. \tag{2.1.18}$$

2.2 Frequency domain Maxwell's equations

Maxwell's equations in the time domain can be simplified with no (or minimal) loss of generality using analytical techniques. In most problems, one is

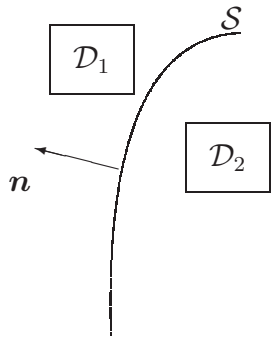

Figure 2.1: Interface between two media with different electromagnetic properties.

interested in the behaviour of a time-invariant configuration with linear and causal media. In these cases, one can advantageously describe the problem via its Laplace domain representation, which is obtained by applying the Laplace transform with respect to time. From this representation, we can easily go to the frequency domain representation of Maxwell's equations.

2.2.1 Maxwell's equations in the Laplace domain and in steady-state

In the Laplace domain representation, the dependence on the time coordinate is transformed into a dependence on the Laplace parameter s. In addition, temporal differentiation is transformed into multiplication by s, and convolution in the time domain turns into multiplication in the Fourier domain.

Take the electric field strength $\mathbf{E}(\mathbf{x}, t)$ as an example of an electromagnetic quantity that is causally related to a source which is switched on at instant $t = t_0$. The Laplace transform with respect to time of $\mathbf{E}(\mathbf{x}, t)$ is then defined

as

$$\hat{\mathbf{E}}(\mathbf{x}, s) = \mathcal{L}_t\{\mathbf{E}(\mathbf{x}, t)\} = \int_{t_0}^{\infty} \mathbf{E}(\mathbf{x}, t) \exp(-st) \mathrm{d}t \quad \text{for } \mathrm{Re}\{s\} > s_0 \geq 0, \tag{2.2.1}$$

where s denotes the complex Laplace transform parameter and $\hat{\mathbf{E}}$ is an analytic function, i.e. differentiable with respect to s, in the right half of the complex s-plane $\mathrm{Re}\{s\} > s_0 \geq 0$. Applying the Laplace transform to Maxwell's equations, we obtain

$$-\boldsymbol{\nabla} \times \hat{\mathbf{H}} + \hat{\mathbf{J}} + s\hat{\mathbf{D}} = -\hat{\mathbf{J}}^{\mathrm{ext}} \tag{2.2.2}$$

and

$$\boldsymbol{\nabla} \times \hat{\mathbf{E}} + s\hat{\mathbf{B}} = -\hat{\mathbf{K}}^{\mathrm{ext}}. \tag{2.2.3}$$

Steady-State Analysis

In a steady-state analysis, all electromagnetic field quantities are taken to depend sinusoidally on time with a common angular frequency ω. To each purely real space-time field quantity $f(\mathbf{x}, t)$ we can then associate a complex phasor $\hat{f}(\mathbf{x}, \mathrm{j}\omega)$ and a common time factor $\exp(\mathrm{j}\omega t)$. The phasor $\hat{f}$ and the corresponding original space-time function f are related by

$$f(\mathbf{x}, t) = \mathrm{Re}\left[\hat{f}(\mathbf{x}, \mathrm{j}\omega) \exp(\mathrm{j}\omega t)\right]$$

and substitution of these representations for the electromagnetic field quantities leads to

$$-\boldsymbol{\nabla} \times \hat{\mathbf{H}} + \hat{\mathbf{J}} + \mathrm{j}\omega\hat{\mathbf{D}} = -\hat{\mathbf{J}}^{\mathrm{ext}} \tag{2.2.4}$$

and

$$\boldsymbol{\nabla} \times \hat{\mathbf{E}} + \mathrm{j}\omega\hat{\mathbf{B}} = -\hat{\mathbf{K}}^{\mathrm{ext}}. \tag{2.2.5}$$

Comparing these equations with Eqs. (2.2.2) and (2.2.3), we conclude that a steady-state analysis can be interpreted as the limiting case of a Laplace transform analysis with $s = \lim_{\delta \downarrow 0}(\delta + \mathrm{j}\omega)$.

Finally, using the constitutive relations of Eqs. (2.1.15) and (2.1.16) in the above equations, we end up with

$$-\boldsymbol{\nabla} \times \hat{\mathbf{H}} + +\sigma\hat{\mathbf{E}} + \mathrm{j}\omega\varepsilon\hat{\mathbf{E}} = -\hat{\mathbf{J}}^{\mathrm{ext}} \tag{2.2.6}$$

and

$$\boldsymbol{\nabla} \times \hat{\mathbf{E}} + \mathrm{j}\omega\mu_0\hat{\mathbf{H}} = -\hat{\mathbf{K}}^{\mathrm{ext}}. \tag{2.2.7}$$

These equations will serve as a starting point in the analysis that follows in subsequent chapters.

2.3 Time Fourier-transform domain field reciprocity theorem

In this section the time Fourier-transform domain reciprocity theorem or Lorentz's reciprocity theorem [20] is discussed. A reciprocity relation interrelates in a specific manner the field quantities of two non-identical physical states that can occur in one and the same (bounded) domain in space. Let this domain be denoted by $\mathcal{D}$ with an enclosing surface $\partial\mathcal{D}$. The unit vector along the normal to $\partial\mathcal{D}$ is denoted by $\boldsymbol{n}$ and points away from $\mathcal{D}$. The complement of $\mathcal{D} \cup \partial\mathcal{D}$ in $\mathbb{R}^3$ is denoted by $\mathcal{D}'$. The two electromagnetic states that can occur in the domain $\mathcal{D}$ are referred to as states A and B Table 2.2.

	State A	State B
Field state	$\{\hat{\mathbf{E}}^{\mathrm{A}}, \hat{\mathbf{H}}^{\mathrm{A}}\}(\mathbf{x}, \mathrm{j}\omega)$	$\{\hat{\mathbf{E}}^{\mathrm{B}}, \hat{\mathbf{H}}^{\mathrm{B}}\}(\mathbf{x}, \mathrm{j}\omega)$
Material state	$\{\sigma^{\mathrm{A}}, \varepsilon^{\mathrm{A}}, \underline{\boldsymbol{\mu}}^{\mathrm{A}}\}$	$\{\sigma^{\mathrm{B}}, \varepsilon^{\mathrm{B}}, \underline{\boldsymbol{\mu}}^{\mathrm{B}}\}$
Source state	$\{\hat{\mathbf{J}}^{\mathrm{A}}, \hat{\mathbf{K}}^{\mathrm{A}}\}(\mathbf{x}, \mathrm{j}\omega)$	$\{\hat{\mathbf{J}}^{\mathrm{B}}, \hat{\mathbf{K}}^{\mathrm{B}}\}(\mathbf{x}, \mathrm{j}\omega)$

Table 2.2: The two electromagnetic states in the domain $\mathcal{D}$ in the time Laplace transform domain reciprocity theorem.

Since we want to apply the Lorentz reciprocity theorem to electromagnetic fields in a MRI environment, we assume the conductivity and permeability to be scalars, while the permeability consists of an anisotropic tensorial form at the location of the RF-excited magnetic moments that degenerates to a scalar form outside the illuminated region. Neither the media nor the sources present in the two states need be the same. State A is characterized by the electromagnetic field

$$\{\hat{\mathbf{E}}, \hat{\mathbf{H}}\}(\mathbf{x}, \mathrm{j}\omega) = \{\hat{\mathbf{E}}^{\mathrm{A}}, \hat{\mathbf{H}}^{\mathrm{A}}\}(\mathbf{x}, \mathrm{j}\omega), \tag{2.3.1}$$

together with the constitutive parameters

$$\{\sigma, \varepsilon, \underline{\boldsymbol{\mu}}\}(\mathbf{x}) = \{\sigma^{\mathrm{A}}, \varepsilon^{\mathrm{A}}, \underline{\boldsymbol{\mu}}^{\mathrm{A}}\}(\mathbf{x}), \tag{2.3.2}$$

and the volume source distributions

$$\{\hat{\mathbf{J}}, \hat{\mathbf{K}}\}(\mathbf{x}, \mathrm{j}\omega) = \{\hat{\mathbf{J}}^{\mathrm{A}}, \hat{\mathbf{K}}^{\mathrm{A}}\}(\mathbf{x}, \mathrm{j}\omega). \tag{2.3.3}$$

The time Fourier-transform domain electromagnetic field of state A satisfies the partial differential equations

$$-\boldsymbol{\nabla} \times \hat{\mathbf{H}}^{\mathrm{A}} + \sigma^{\mathrm{A}} \hat{\mathbf{E}}^{\mathrm{A}} + \mathrm{j}\omega\varepsilon^{\mathrm{A}} \hat{\mathbf{E}}^{\mathrm{A}} = -\hat{\mathbf{J}}^{\mathrm{A}}, \tag{2.3.4}$$

$$\boldsymbol{\nabla} \times \hat{\mathbf{E}}^{\mathrm{A}} + \mathrm{j}\omega \underline{\boldsymbol{\mu}}^{\mathrm{A}} \hat{\mathbf{H}}^{\mathrm{A}} = -\hat{\mathbf{K}}^{\mathrm{A}}. \tag{2.3.5}$$

Similarly, state B is characterized by the electromagnetic field

$$\{\hat{\mathbf{E}}, \hat{\mathbf{H}}\}(\mathbf{x}, \mathrm{j}\omega) = \{\hat{\mathbf{E}}^{\mathrm{B}}, \hat{\mathbf{H}}^{\mathrm{B}}\}(\mathbf{x}, \mathrm{j}\omega), \tag{2.3.6}$$

together with the constitutive parameters

$$\{\sigma, \varepsilon, \underline{\boldsymbol{\mu}}\}(\mathbf{x}) = \{\sigma^{\mathrm{B}}, \varepsilon^{\mathrm{B}}, \underline{\boldsymbol{\mu}}^{\mathrm{B}}\}(\mathbf{x}), \tag{2.3.7}$$

and the volume source distributions

$$\{\hat{\mathbf{J}}, \hat{\mathbf{K}}\}(\mathbf{x}, \mathrm{j}\omega) = \{\hat{\mathbf{J}}^{\mathrm{B}}, \hat{\mathbf{K}}^{\mathrm{B}}\}(\mathbf{x}, \mathrm{j}\omega). \tag{2.3.8}$$

The time Fourier-transform domain electromagnetic field of state B satisfies the partial differential equations

$$-\boldsymbol{\nabla} \times \hat{\mathbf{H}}^{\mathrm{B}} + \sigma^{\mathrm{B}} \hat{\mathbf{E}}^{\mathrm{B}} + \mathrm{j}\omega\varepsilon^{\mathrm{B}} \hat{\mathbf{E}}^{\mathrm{B}} = -\hat{\mathbf{J}}^{\mathrm{B}}, \tag{2.3.9}$$

$$\boldsymbol{\nabla} \times \hat{\mathbf{E}}^{\mathrm{B}} + \mathrm{j}\omega \underline{\boldsymbol{\mu}}^{\mathrm{B}} \hat{\mathbf{H}}^{\mathrm{B}} = -\hat{\mathbf{K}}^{\mathrm{B}}. \tag{2.3.10}$$

The fundamental interaction quantity between the two states to be considered is the divergence of the vectorial quantity $\boldsymbol{\nabla} \cdot (\hat{\mathbf{E}}^{\mathrm{A}} \times \hat{\mathbf{H}}^{\mathrm{B}} - \hat{\mathbf{E}}^{\mathrm{B}} \times \hat{\mathbf{H}}^{\mathrm{A}})$. Which can be written as

$$\begin{aligned} \boldsymbol{\nabla} \cdot (\hat{\mathbf{E}}^{\mathrm{A}} \times \hat{\mathbf{H}}^{\mathrm{B}} - \hat{\mathbf{E}}^{\mathrm{B}} \times \hat{\mathbf{H}}^{\mathrm{A}}) \;\; = \;\; & -\hat{\mathbf{H}}^{\mathrm{B}} \cdot (\boldsymbol{\nabla} \times \hat{\mathbf{E}}^{\mathrm{A}}) + \hat{\mathbf{E}}^{\mathrm{A}} \cdot (\boldsymbol{\nabla} \times \hat{\mathbf{H}}^{\mathrm{B}}) \\ & + \hat{\mathbf{H}}^{\mathrm{A}} \cdot (\boldsymbol{\nabla} \times \hat{\mathbf{E}}^{\mathrm{B}}) - \hat{\mathbf{E}}^{\mathrm{B}} \cdot (\boldsymbol{\nabla} \times \hat{\mathbf{H}}^{\mathrm{A}}). \end{aligned} \tag{2.3.11}$$

The four terms on the right hand side of Eq. (2.3.11) can be rewritten using

the differential equations (2.3.4), (2.3.5), (2.3.9) and (2.3.10) for the two different states. By collecting the results, we end up with the local form of the time Fourier-transform domain reciprocity theorem for the fields of State A and State B as

$$\begin{aligned} \boldsymbol{\nabla} \cdot (\hat{\mathbf{E}}^{\mathrm{A}} \times \hat{\mathbf{H}}^{\mathrm{B}} - \hat{\mathbf{E}}^{\mathrm{B}} \times \hat{\mathbf{H}}^{\mathrm{A}}) \;\; = \;\; & \mathrm{j}\omega(\hat{\mathbf{H}}^{\mathrm{B}} \cdot \underline{\boldsymbol{\mu}}^{\mathrm{A}} \hat{\mathbf{H}}^{\mathrm{A}} - \hat{\mathbf{H}}^{\mathrm{A}} \cdot \underline{\boldsymbol{\mu}}^{\mathrm{B}} \hat{\mathbf{H}}^{\mathrm{B}}) \\ & - \mathrm{j}\omega(\varepsilon^{\mathrm{A}} - \varepsilon^{\mathrm{B}}) \hat{\mathbf{E}}^{\mathrm{B}} \cdot \hat{\mathbf{E}}^{\mathrm{A}} - (\sigma^{\mathrm{A}} - \sigma^{\mathrm{B}}) \hat{\mathbf{E}}^{\mathrm{B}} \cdot \hat{\mathbf{E}}^{\mathrm{A}} \\ & + \hat{\mathbf{E}}^{\mathrm{A}} \cdot \hat{\mathbf{J}}^{\mathrm{B}} - \hat{\mathbf{E}}^{\mathrm{B}} \cdot \hat{\mathbf{J}}^{\mathrm{A}} - \hat{\mathbf{H}}^{\mathrm{A}} \cdot \hat{\mathbf{K}}^{\mathrm{B}} + \hat{\mathbf{H}}^{\mathrm{A}} \cdot \hat{\mathbf{K}}^{\mathrm{A}}. \end{aligned} \tag{2.3.12}$$

Integration of Eq. (2.3.12) over the domain $\mathcal{D}$ with boundary $\partial\mathcal{D}$ and the use of Gauss' integral theorem in the resulting left-hand side leads to

$$\begin{aligned} & \iint_{\mathbf{x} \in \partial\mathcal{D}} \mathbf{n} \cdot (\hat{\mathbf{E}}^{\mathrm{A}} \times \hat{\mathbf{H}}^{\mathrm{B}} - \hat{\mathbf{E}}^{\mathrm{B}} \times \hat{\mathbf{H}}^{\mathrm{A}}) \, \mathrm{d}A = \\ & \quad \iiint_{\mathbf{x} \in \mathcal{D}} \big[\mathrm{j}\omega(\hat{\mathbf{H}}^{\mathrm{B}} \cdot \underline{\boldsymbol{\mu}}^{\mathrm{A}} \hat{\mathbf{H}}^{\mathrm{A}} - \hat{\mathbf{H}}^{\mathrm{A}} \cdot \underline{\boldsymbol{\mu}}^{\mathrm{B}} \hat{\mathbf{H}}^{\mathrm{B}}) - \mathrm{j}\omega(\varepsilon^{\mathrm{A}} - \varepsilon^{\mathrm{B}}) \hat{\mathbf{E}}^{\mathrm{B}} \cdot \hat{\mathbf{E}}^{\mathrm{A}} \\ & \quad - (\sigma^{\mathrm{A}} - \sigma^{\mathrm{B}}) \hat{\mathbf{E}}^{\mathrm{B}} \cdot \hat{\mathbf{E}}^{\mathrm{A}} \big] \, \mathrm{d}V + \iiint_{\mathbf{x} \in \mathcal{D}} \big[\hat{\mathbf{E}}^{\mathrm{A}} \cdot \hat{\mathbf{J}}^{\mathrm{B}} - \hat{\mathbf{E}}^{\mathrm{B}} \cdot \hat{\mathbf{J}}^{\mathrm{A}} \\ & \quad - \hat{\mathbf{H}}^{\mathrm{A}} \cdot \hat{\mathbf{K}}^{\mathrm{B}} + \hat{\mathbf{H}}^{\mathrm{B}} \cdot \hat{\mathbf{K}}^{\mathrm{A}} \big] \, \mathrm{d}V, \end{aligned} \tag{2.3.13}$$

which is the global form of the time Fourier-transform domain reciprocity theorem. It is noted that the first three terms on the right-hand side of Eq. (2.3.12), as well as the first integral on the right-hand side of Eq. (2.3.13), vanish in case the media in the two states are chosen such that $\sigma^{\mathrm{A}} = \sigma^{\mathrm{B}}$, $\varepsilon^{\mathrm{A}} = \varepsilon^{\mathrm{B}}$ and $\underline{\boldsymbol{\mu}}^{\mathrm{A}} = (\underline{\boldsymbol{\mu}}^{\mathrm{B}})^{T}$. If in addition the source distributions vanish in some domain, the corresponding local and global interactions are zero in that domain.

Chapter 3

Basic Magnetic Resonance Imaging

After our short review of basic electromagnetic theory, we now focus on the MRI scanner itself. A complete description of such a scanner is obviously outside the scope of this thesis. We therefore only consider some main aspects of Magnetic Resonance Imaging.

3.1 Antennas in an MRI system

Presently, MRI is a diagnostics tool of great importance and it is becoming more and more popular, since it uses nonionizing radiation that is much safer than, for example, X-ray radiation used in X-ray tomography.

Loosely speaking, an MRI machine has three major components, namely, a superconducting magnet, a set of three gradient coils, and a set of RF transmit/receiver coils (see Fig. 3.1).

The superconducting coil generates the strong background field used in MRI. At 3 tesla, it is roughly 60000 times stronger than the Earth's magnetic field. If a piece of matter is placed inside the background field, the protons start to precess at a frequency that is linearly related to the magnitude of the background field. This frequency is called the Larmor frequency and is equal to 128 MHz at three tesla.

The gradient coils also produce a magnetic field, but this field is much smaller than the one produced by the superconducting coil. The gradient coils make it possible to spatially vary the magnetic field strength, and thus

the precession speed, and consequently we can select a certain region for imaging. Finally, an RF antenna operating at the Larmor frequency is used to excite the proton spins and after this antenna has been switched off, a receiving antenna measures the electromagnetic signals that are transmitted as the protons return to equilibrium.

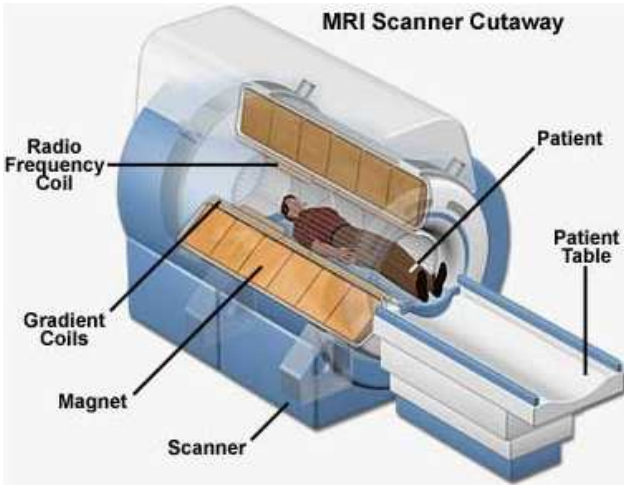

Figure 3.1: Overview of the main components of an MRI scanner

3.2 Effects of the external magnetic fields on protons

As mentioned earlier, there is a strong magnetic field inside the MRI scanner. This magnetic field will interact with the protons in the body. The protons are charged particles and rotate around an internal axis a thus have an angular momentum and a magnetic moment. Under normal circumstances, the protons are randomly distributed as illustrated in Fig. 3.2, left. Because the spins are all randomly distributed, the resulting magnetic moment of the whole body will be zero. When the protons are placed in a strong magnetic field, however, two important phenomena occur.

First, the protons start to align as shown on the right-hand side of Fig. 3.2. This alignment can occur in two ways, namely, parallel and anti-parallel to the applied magnetic field.

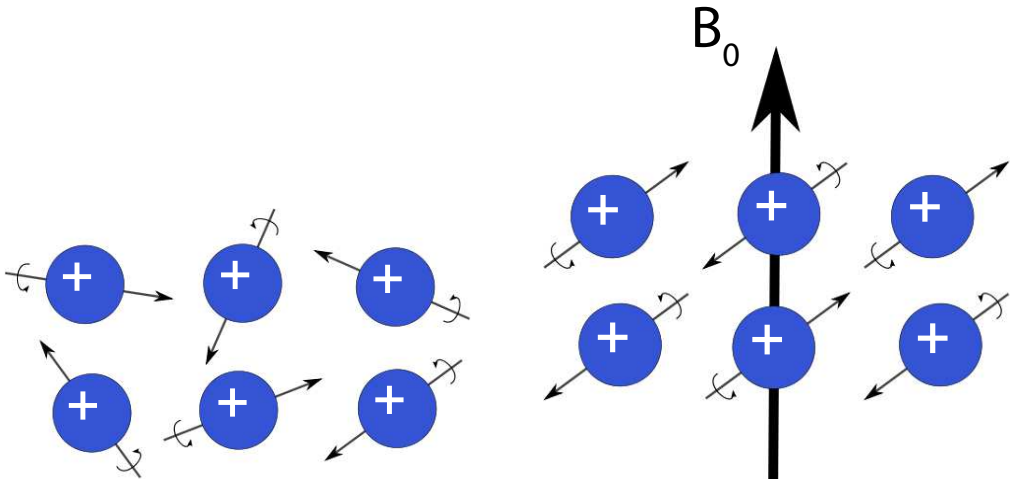

Figure 3.2: The normal randomly distributed protons are alligned by applying a magnetic field, the allignment can be parallel or anti-parallel

The number of protons in parallel and anti-parallel is dependent on the strength of the applied magnetic field. Protons in the anti-parallel state will have a higher energy level than protons in the parallel state. The energy difference between the two states is given by [21]

$$\Delta E = \frac{\gamma h B_0}{2\pi}, \tag{3.2.1}$$

where h is Plank's constant ($6.63 \cdot 10^{-34}\ Js$) and B_0 is the magnitude of the applied background field. Furthermore, the ratio of the number of anti-parallel and parallel protons is

$$\frac{N_{\text{anti-parallel}}}{N_{\text{parallel}}} = \exp\left(-\frac{\Delta E}{kT}\right) = \exp\left(-\frac{\gamma h B_0}{2\pi kT}\right), \tag{3.2.2}$$

where k is the Boltzmann's constant ($1.38 \cdot 10^{-23}\ J/K$) and T is the temperature in Kelvin. Because the argument of the exponent is very small, we have $\exp(-x) \approx 1 - x$ and the above simplifies to

$$\frac{N_{\text{anti-parallel}}}{N_{\text{parallel}}} = 1 - \frac{\gamma h B_0}{2\pi kT}. \tag{3.2.3}$$

The total signal that is received by the MRI scanner is dependent on the difference of population of the two energy levels. Specifically, we have

$$N_{\text{parallel}} - N_{\text{anti parallel}} = N_{\text{total}} \frac{\gamma h B_0}{4\pi kT}, \tag{3.2.4}$$

where N_{total} is the total number of protons. Note that the received signal is only dependent on the difference between the number of parallel and anti-parallel protons and not on the total number of protons.

The second phenomenon that occurs is that the angular momentum will also change according to the strength of the magnetic field that is applied. The angular momentum (rotation around its own axis) is dependent on the imposed magnetic field through the gyromagnetic ratio γ. For protons, the gyromagnetic ratio is about $267.54 \cdot 10^6$ rad $\text{s}^{-1}\text{T}^{-1}$.

As can be seen in Fig. 3.2, the center axes of the protons are under an angle compared to the magnetic field. This angle is constant and approximately 54.7°. Since the proton is rotating around its own axis, it induces another rotation. This is a rotation of the proton around the axis of the magnetic field. This can be visualized best by thinking of a spinning top (see Fig. 3.3). The proton rotates about its own axis, but before it "falls" it starts to rotate around the vertical axis.

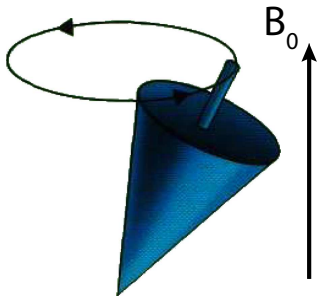

Figure 3.3: Spinning top with two rotations, one around its own axis and a precession around a vertical axis.

The frequency of the rotation around the direction of the magnetic field is called the precession or Larmor frequency. This frequency is dependent on how fast the protons are spinning around their own axis. This makes the precession frequency also dependent on the magnetic field. For a three tesla background field, the precession frequency is

$$f^{3\text{T}} = \frac{\omega}{2\pi} = \frac{\gamma B_0}{2\pi} = \frac{267.54 \cdot 10^6 \cdot 3}{2\pi} = 127.7 \text{ MHz}. \tag{3.2.5}$$

The cumulative effect of all the parallel and anti-parallel spinning protons can be taken into account macroscopically through a magnetization vector $\mathbf{M}$

as illustrated in Fig. 3.4. Part of the parallel spins will be cancelled out by the anti-parallel spins, but since there is a larger amount of parallel spins, a net magnetization results in the direction of the magnetic field. Taking the z-direction to be the direction of the background magnetic field, we have

$$M_z = M_0 = V^{-1} \sum_{\mathrm{n=1}}^{\mathrm{N_{total}}} \mu_{z,n} = \frac{\gamma h}{4\pi}(N_{\mathrm{parallel}} - N_{\mathrm{anti\text{-}parallel}}) = \frac{\gamma^2 h^2 B_0 N_{\mathrm{total}}}{16\pi^2 kT}, \tag{3.2.6}$$

where V is a volume small enough that external fields are constant over V.

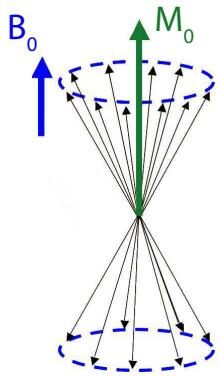

Figure 3.4: Formation of the macroscopic magnetization. Part of the parallel and anti-parallel spins cancel out. Since the number of protons with a parallel spin is larger than the number of anti-parallel spins, a net magnetization vector $M_z = M_0$ results in the parallel direction.

The radio frequency pulse

To change the magnetization, energy has to be transferred from an electromagnetic energy source (antenna) to the protons. This can be realized by transmitting a radio frequency pulse. Energy transfer is only possible when the protons and the radio frequency pulse have the same frequency. This means that for 3 tesla the RF pulse must have a frequency of 127.7 MHz or else little to no energy transfer is possible. If the protons and the RF pulse have the same frequency they are in "resonance".

By applying the RF pulse the magnetization can be flipped. The RF magnetic field is called the $\mathbf{B}_1$ field, and this field produces a torque that flips the magnetization into the transverse plane.

This field can be divided in two rotating components called the B_1^+ and the B_1^-. The B_1^+ is rotating in the clockwise direction and the B_1^- is rotating in the anti-clockwise direction and are defined as

$$\hat{B}_1^+ = \frac{\hat{B}_{1;x} + \mathrm{j}\hat{B}_{1;y}}{2}, \tag{3.2.7}$$

$$\hat{B}_1^- = \frac{\hat{B}_{1;x} - \mathrm{j}\hat{B}_{1;y}}{2}. \tag{3.2.8}$$

The $\hat{B}_1^-$ component of the magnetic field strength describes the behaviour of the magnetic field in the receiving state of the MRI scanner, while the $\hat{B}_1^+$ component can interact effectively with the spins of the protons and may push the magnetization into the transverse plane during the exiting state of the scanner. How much the magnetization is tipped into the transverse plane is determined by the so-called flip angle

$$\alpha = \gamma|\hat{\mathbf{B}}_1|\tau_{\mathbf{B}_1}, \tag{3.2.9}$$

where τ_{B_1} is the duration of the RF pulse. When the magnetization is tipped 90° down there is no magnetization left in the B_0 direction and the magnetization is completely located in the transverse plane.

Signal detection

When the magnetization is flipped, the protons want to return to equilibrium with a magnetization in the direction of the $\mathbf{B}_0$ field. This process, called relaxation, is described by the so-called Bloch equations [19] and consists of essentially two relaxation phenomena. The first influences magnetization in the z-direction only and is called T_1 or spin-lattice relaxation time, while the second is called T_2 relaxation or spin-spin relaxation relaxation time which relates to the decay of magnetization in the transverse plane after excitation with a RF pulse (only M_x and M_y are affected).

From the Bloch equations it follows that for T_1 relaxation, the z-component of the magnetization is given by

$$M_z(t) = M_0 \cos\alpha + (M_0 - M_0 \cos\alpha)\left[1 - \exp\left(-\frac{t}{T_1}\right)\right], \tag{3.2.10}$$

where M_0 is the magnitude of the equilibrium static magnetization due to the static magnetic field $\mathbf{B}_0$. The behaviour of this T_1 relaxation function is shown in Fig. 3.5 and is called the T_1 curve.

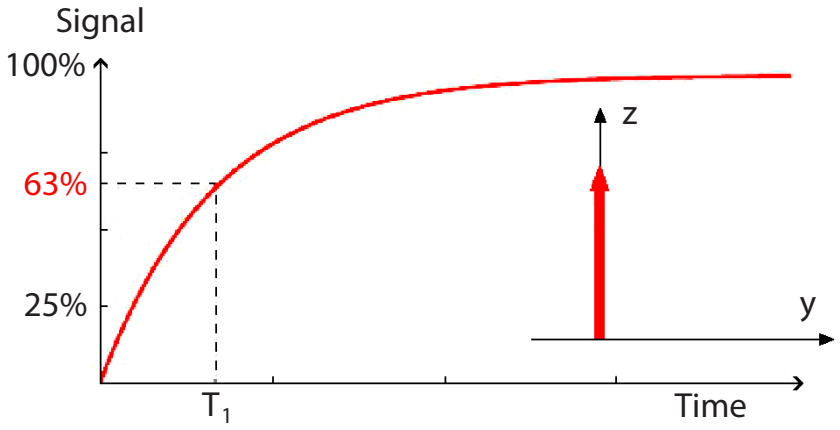

Figure 3.5: T_1 relaxation of the magnetization in the direction of the applied magnetic field.

The T_1 time is defined as the point on the curve where the magnetization is restored to 63% of the relaxed value.

For T_2 relaxation, we have for the y-component of the magnetization

$$M_y(t) = M_0 \sin\alpha \exp\left(-\frac{t}{T_2}\right) \tag{3.2.11}$$

The behaviour of T_2 relaxation is shown in Fig. 3.6 and is called the T_2 curve.

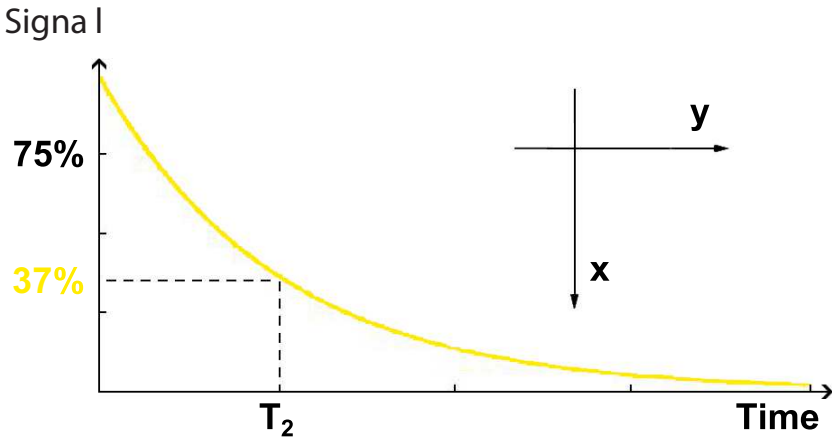

Figure 3.6: T_2 relaxation of the magnetization in the transverse plane compaired with the direction of the applied magnetic field.

The T_2 time is defined as the point on the curve where 37% magnetization of the maximum value is left.

3.3 B field description

For electromagnetic fields present in MRI we have at the location of induced Magnetic Resonance due to the externally imposed RF field radiating at the Larmor frequency ω_0 according to Ibrahim [22] for the tensorial permeability

$$\hat{\mathbf{B}}(\mathbf{x}, \mathrm{j}\omega_0) = \mu \begin{bmatrix} 1 - \mathrm{j}\gamma M_0 T_2/2 & -\gamma M_0 T_2/2 & 0 \\ \gamma M_0 T_2/2 & 1 - \mathrm{j}\gamma M_0 T_2/2 & 0 \\ 0 & 0 & 1 \end{bmatrix} \hat{\mathbf{H}}(\mathbf{x}, \mathrm{j}\omega_0). \tag{3.3.1}$$

Outside the region of induced Magnetic resonance when $\omega \neq \omega_0$ the tensorial permeability $\underline{\boldsymbol{\mu}}$ reduces to the scalar permeability μ as the matrix in Eq. (3.3.1) changes into the unit matrix, which yields

$$\hat{\mathbf{B}}(\mathbf{x}, \mathrm{j}\omega) = \mu \hat{\mathbf{H}}(\mathbf{x}, \mathrm{j}\omega), \text{ when } \omega \neq \omega_0. \tag{3.3.2}$$

3.3.1 The electromagnetic RF field in the excitation state

In this section we consider the electromagnetic field with frequency ω_0 that excites the magnetic contrast sources due to the tensorial permeability de-

fined in Eq. (3.3.1). We will employ Lorentz's reciprocity theorem as defined in Eq. (2.3.13) in order to obtain representations for the electromagnetic field inside the human body when the body is illuminated by an electromagnetic field operating at the Larmor frequency ω_0, we distinguish two different states in Lorentz's reciprocity theorem. The excitation state is the state where the generated electromagnetic fields $\{\hat{\mathbf{E}}^{\mathrm{e}}, \hat{\mathbf{H}}^{\mathrm{e}}\}$ in the entire domain $\mathbb{R}$ are excited by a current source distribution $\hat{\mathbf{J}}^{\mathrm{e}}$ inside a domain $\mathcal{S}$ (i.e. the domain of the exciting RF birdcage antenna) that illuminates the body that has a certain permittivity, conductivity and permeability distribution. While, the other state with electromagnetic fields $\{\hat{\mathbf{E}}^{\mathrm{b}}, \hat{\mathbf{H}}^{\mathrm{b}}\}$ is the field that is present in a homogeneous background medium and is generated by an electric current source or an magnetic current source. We can refer to this state as a Green's state. When we use an electric current point source in this Green's state, we will obtain in Lorentz's reciprocity theorem an integral equation representation for the electric field $\hat{\mathbf{E}}^{\mathrm{e}}$. On the other hand when we use a magnetic current point source in this Green's state, we will obtain in Lorentz's reciprocity theorem an integral equation representation for the magnetic field $\hat{\mathbf{H}}^{\mathrm{e}}$.

Since in the excitation state we want to know the magnetic field at the location of the induced magnetic resonance, we choose for the Green's state an excitation by an unit magnetic current point source located in a homogeneous medium with permittivity ε_{b}, conductivity σ_{b} and permeability μ_{b}. For the two states in the excitation state we then have in Lorentz's reciprocity theorem (2.3.13),

$$\{\hat{\mathbf{E}}^{\mathrm{A}}, \hat{\mathbf{H}}^{\mathrm{A}}\} = \{\hat{\mathbf{E}}^{\mathrm{e}}, \hat{\mathbf{H}}^{\mathrm{e}}\} \tag{3.3.3}$$

$$\{\hat{\mathbf{J}}^{\mathrm{A}}, \hat{\mathbf{K}}^{\mathrm{A}}\} = \{\hat{\mathbf{J}}^{\mathrm{e}}, \mathbf{0}\}, \text{ when } \mathbf{x} \in \mathcal{S} \tag{3.3.4}$$

$$\varepsilon^{\mathrm{A}} = \varepsilon^{\mathrm{e}}(\mathbf{x}) \tag{3.3.5}$$

$$\sigma^{\mathrm{A}} = \sigma^{\mathrm{e}}(\mathbf{x}) \tag{3.3.6}$$

$$\underline{\hat{\boldsymbol{\mu}}}^{\mathrm{A}} = \underline{\hat{\boldsymbol{\mu}}}^{\mathrm{e}}(\mathbf{x}, \mathrm{j}\omega_0), \tag{3.3.7}$$

in which $\underline{\hat{\boldsymbol{\mu}}}^{\mathrm{e}}(\mathbf{x}, \mathrm{j}\omega_0)$ is defined by Eq. (3.3.1), which reduces to a scalar permeability $\mu^{\mathrm{e}}(\mathbf{x})$ when $\omega \neq \omega_0$. The Green's state for a unit magnetic current point source $\hat{\mathbf{K}}^{\mathrm{B}} = \delta(\mathbf{x} - \mathbf{x}')\mathbf{u}$, where $\delta(\mathbf{x} - \mathbf{x}')$ represents the three-dimensional unit impulse (Dirac distribution) operative at $\mathbf{x} = \mathbf{x}'$ and $\mathbf{u}$ represents the unit amplitude vector with $u_1 = u_2 = u_3 = 1$. The unit magnetic source is located inside the homogeneous domain with permittivity

$\varepsilon_{\rm b}$, conductivity $\sigma_{\rm b}$ and permeability $\mu_{\rm b}$, which yields for state B

$$\begin{aligned}\{\hat{\mathbf{E}}^{\rm B},\hat{\mathbf{H}}^{\rm B}\} &= \{\hat{\mathbf{E}}^{\mathbf{K};{\rm b}},\hat{\mathbf{H}}^{\mathbf{K};{\rm b}}\}(\mathbf{x},\mathbf{x}',{\rm j}\omega) &(3.3.8)\\ &= \{\hat{\underline{\mathbf{G}}}^{\mathbf{EK}},\hat{\underline{\mathbf{G}}}^{\mathbf{HK}}\}(\mathbf{x},\mathbf{x}',{\rm j}\omega)\mathbf{u}\\ \{\hat{\mathbf{J}}^{\rm B},\hat{\mathbf{K}}^{\rm B}\} &= \{\mathbf{0},\delta(\mathbf{x}-\mathbf{x}')\mathbf{u}\} &(3.3.9)\\ \varepsilon^{\rm B} &= \varepsilon_{\rm b} &(3.3.10)\\ \sigma^{\rm B} &= \sigma_{\rm b} &(3.3.11)\\ \underline{\boldsymbol{\mu}}^{\rm B} &= \mu_{\rm b}\underline{\mathbf{I}}, &(3.3.12)\end{aligned}$$

where $\hat{\underline{\mathbf{G}}}^{\mathbf{EK}}$ represents the electric-field/magnetic-current Green's tensor, $\hat{\underline{\mathbf{G}}}^{\mathbf{HK}}$ represents the magnetic-field/magnetic-current Green's tensor. Similarly, the Green's tensor $\hat{\underline{\mathbf{G}}}^{\mathbf{EJ}}$ represents the electric-field/electric-current Green's tensor and $\hat{\underline{\mathbf{G}}}^{\mathbf{HJ}}$ represents the magnetic-field/electric-current Green's tensor. Finally, $\underline{\mathbf{I}}$ represents the unit tensor and all tensors are of rank 3.

Application of Lorentz's reciprocity theorem Eq. (2.3.13) in which we let $\partial\mathcal{D}$ extend to infinity (unbounded domain) yields,

$$\begin{aligned}\iiint_{\mathbf{x}\in\mathcal{D}}[{\rm j}\omega(\hat{\mathbf{H}}^{\rm B}\cdot\hat{\underline{\boldsymbol{\mu}}}^{\rm A}\hat{\mathbf{H}}^{\rm A} &- \hat{\mathbf{H}}^{\rm A}\cdot\underline{\boldsymbol{\mu}}^{\rm B}\hat{\mathbf{H}}^{\rm B}) - {\rm j}\omega(\varepsilon^{\rm A}-\varepsilon^{B})\hat{\mathbf{E}}^{\rm B}\cdot\hat{\mathbf{E}}^{\rm A}\\ &- (\sigma^{\rm A}-\sigma^{\rm B})\hat{\mathbf{E}}^{\rm B}\cdot\hat{\mathbf{E}}^{\rm A}+\hat{\mathbf{E}}^{\rm A}\cdot\hat{\mathbf{J}}^{\rm B}-\hat{\mathbf{E}}^{\rm B}\cdot\hat{\mathbf{J}}^{\rm A}\\ &- \hat{\mathbf{H}}^{\rm A}\cdot\hat{\mathbf{K}}^{\rm B}+\hat{\mathbf{H}}^{\rm B}\cdot\hat{\mathbf{K}}^{\rm A}]\,{\rm d}V=0 \qquad (3.3.13)\end{aligned}$$

since according to the radiation condition of the electromagnetic fields at infinity, the contribution of the surface integral vanishes.

Substitution of the fields and sources of the corresponding states in Eq. (3.3.13), using the fact that for a general field/source vector $\hat{\mathbf{F}}$

$$\hat{\underline{\mathbf{G}}}^{\mathbf{EK}}(\mathbf{x},\mathbf{x}',{\rm j}\omega)\mathbf{u}\cdot\hat{\mathbf{F}}=\mathbf{u}\cdot(\hat{\underline{\mathbf{G}}}^{\mathbf{EK}})^{T}(\mathbf{x}',\mathbf{x},{\rm j}\omega)\hat{\mathbf{F}}=-\mathbf{u}\cdot(\hat{\underline{\mathbf{G}}}^{\mathbf{HJ}})^{T}(\mathbf{x}',\mathbf{x},{\rm j}\omega)\hat{\mathbf{F}}, \qquad (3.3.14)$$

and

$$\hat{\underline{\mathbf{G}}}^{\mathbf{HK}}(\mathbf{x},\mathbf{x}',{\rm j}\omega)\mathbf{u}\cdot\hat{\mathbf{F}}=\mathbf{u}\cdot(\hat{\underline{\mathbf{G}}}^{\mathbf{HK}})^{T}(\mathbf{x}',\mathbf{x},{\rm j}\omega)\hat{\mathbf{F}}, \qquad (3.3.15)$$

holds, we obtain

$$\begin{aligned}\hat{\mathbf{H}}^{\rm e}(\mathbf{x}') &= \iiint_{\mathbf{x}\in\mathcal{V}}{\rm j}\omega(\hat{\underline{\mathbf{G}}}^{\mathbf{HK}})^{T}(\mathbf{x}',\mathbf{x},{\rm j}\omega)(\hat{\underline{\boldsymbol{\mu}}}^{\rm e}(\mathbf{x})-\mu_{\rm b}\underline{\mathbf{I}})\hat{\mathbf{H}}^{\rm e}(\mathbf{x})\\ &\quad+[{\rm j}\omega(\varepsilon^{\rm e}(\mathbf{x})-\varepsilon_{\rm b})+(\sigma^{\rm e}(\mathbf{x})-\sigma_{\rm b})](\hat{\underline{\mathbf{G}}}^{\mathbf{HJ}})^{T}(\mathbf{x}',\mathbf{x},{\rm j}\omega)\hat{\mathbf{E}}^{\rm e}(\mathbf{x})\,{\rm d}V\\ &\quad+\iiint_{\mathbf{x}\in\mathcal{S}}(\hat{\underline{\mathbf{G}}}^{\mathbf{HJ}})^{T}(\mathbf{x}',\mathbf{x},{\rm j}\omega)\hat{\mathbf{J}}^{\rm e}(\mathbf{x})\,{\rm d}V,\quad\text{for }\mathbf{x}'\in\mathbb{R}^3, \qquad (3.3.16)\end{aligned}$$

in which the domain $\mathcal{V}$ is the domain that contains the illuminated human body and the domain $\mathcal{S}$ is the domain that contains the illuminating RF antenna. The first expression of Eq. (3.3.16) is the contribution to the exciting magnetic field that is related to the energy transfer to the protons, the second expression is due to the electric contrast of the body (and pads) which cause the inhomogeneities in the transmitted magnetic field by loading the domain with the body and the third expression is the field generated by the antenna. Note that the second expression of the equation is proof why the dielectric pads that only have a electric contrast still influence the magnetic field.

3.3.2 The electromagnetic RF field in the receiving state

In this section we consider the electromagnetic field with frequency ω_0 that is received by receiving antennas and is excited by the magnetic contrast sources due to the tensorial permeability defined in Eq. (3.3.1). We will employ Lorentz's reciprocity theorem as defined in Eq. (2.3.13) in order to obtain representations for the electromagnetic field at the receiving antennas. Again we distinguish two different states in Lorentz's reciprocity theorem. The receiving state is the state where the emitted electromagnetic fields $\{\hat{\mathbf{E}}^{\mathrm{e}}, \hat{\mathbf{H}}^{\mathrm{e}}\}$ in the entire domain $\mathbb{R}$ are excited by the magnetic contrast source distribution $\hat{\mathbf{K}}^{\mathrm{r}}$ inside a domain $\mathcal{K}$ (i.e. the domain that contains the slice of excited magnetic contrast sources or magnetic moments with Larmor frequency (ω_0) obtained from the excitation state in the previous section,

$$\hat{\mathbf{K}}^{\mathrm{r}}(\mathbf{x}) = \mathrm{j}\omega(\underline{\boldsymbol{\mu}}^{\mathrm{e}}(\mathbf{x}) - \mu_{\mathrm{b}}\underline{\mathbf{I}})\hat{\mathbf{H}}^{\mathrm{e}}(\mathbf{x}), \text{ with } \mathbf{x} \in \mathcal{K}. \tag{3.3.17}$$

While, the other state with electromagnetic fields $\{\hat{\mathbf{E}}^{\mathrm{b}}, \hat{\mathbf{H}}^{\mathrm{b}}\}$ is the field that is present in a homogeneous background medium and is generated by an electric current source or an magnetic current source. We can refer to this state as a Green's state.

Since in the receiving state we want to know the magnetic field at the location of the receiving antennas, we choose for the Green's state an excitation by an unit magnetic current point source located in a homogeneous medium with permittivity ε_{b}, conductivity σ_{b} and permeability μ_{b}. For the two states

in the receiving state we then have in Lorentz's reciprocity theorem (2.3.13),

$$\{\hat{\mathbf{E}}^{\mathrm{A}}, \hat{\mathbf{H}}^{\mathrm{A}}\} = \{\hat{\mathbf{E}}^{\mathrm{r}}, \hat{\mathbf{H}}^{\mathrm{r}}\} \tag{3.3.18}$$

$$\{\hat{\mathbf{J}}^{\mathrm{A}}, \hat{\mathbf{K}}^{\mathrm{A}}\} = \{\mathbf{0}, \hat{\mathbf{K}}^{\mathrm{r}}\}, \text{ when } \mathbf{x} \in \mathcal{K} \tag{3.3.19}$$

$$\varepsilon^{\mathrm{A}} = \varepsilon^{\mathrm{r}}(\mathbf{x}) \tag{3.3.20}$$

$$\sigma^{\mathrm{A}} = \sigma^{\mathrm{r}}(\mathbf{x}) \tag{3.3.21}$$

$$\underline{\boldsymbol{\mu}}^{\mathrm{A}} = \mu_{\mathrm{b}}\underline{\mathbf{I}}. \tag{3.3.22}$$

The Green's state for a unit magnetic current point source $\hat{\mathbf{K}}^{\mathrm{B}} = \delta(\mathbf{x} - \mathbf{x}')\mathbf{u}$, where $\delta(\mathbf{x} - \mathbf{x}')$ represents the three-dimensional unit impulse (Dirac distribution) operative at $\mathbf{x} = \mathbf{x}'$ and $\mathbf{u}$ represents the unit amplitude vector with $u_1 = u_2 = u_3 = 1$. The unit magnetic source is located inside the homogeneous domain with permittivity ε_{b}, conductivity σ_{b} and permeability μ_{b}, which yields for state B

$$\{\hat{\mathbf{E}}^{\mathrm{B}}, \hat{\mathbf{H}}^{\mathrm{B}}\} = \{\hat{\mathbf{E}}^{\mathbf{K};\mathrm{b}}, \hat{\mathbf{H}}^{\mathbf{K};\mathrm{b}}\}(\mathbf{x}, \mathbf{x}', \mathrm{j}\omega) \tag{3.3.23}$$

$$= \{\hat{\underline{\mathbf{G}}}^{\mathbf{EK}}, \hat{\underline{\mathbf{G}}}^{\mathbf{HK}}\}(\mathbf{x}, \mathbf{x}', \mathrm{j}\omega)\mathbf{u}$$

$$\{\hat{\mathbf{J}}^{\mathrm{B}}, \hat{\mathbf{K}}^{\mathrm{B}}\} = \{\mathbf{0}, \delta(\mathbf{x} - \mathbf{x}')\mathbf{u}\} \tag{3.3.24}$$

$$\varepsilon^{B} = \varepsilon_{\mathrm{b}} \tag{3.3.25}$$

$$\sigma^{\mathrm{B}} = \sigma_{\mathrm{b}} \tag{3.3.26}$$

$$\underline{\boldsymbol{\mu}}^{\mathrm{B}} = \mu_{\mathrm{b}}\underline{\mathbf{I}}. \tag{3.3.27}$$

Substitution of the fields and sources of the corresponding states in Eq. (3.3.13), using the properties for a general field/source vector described in Eqs. (3.3.14) and (3.3.15) results in the following expression for the magnetic field.

$$\begin{aligned}\hat{\mathbf{H}}^{\mathrm{r}}(\mathbf{x}') = &\iiint_{\mathbf{x}\in\mathcal{V}} \hat{\mathbf{E}}^{\mathrm{r}}(\mathbf{x})(\hat{\underline{\mathbf{G}}}^{\mathbf{HK}})^{T}(\mathbf{x}', \mathbf{x}, \mathrm{j}\omega)\big(\mathrm{j}\omega(\varepsilon^{\mathrm{r}}(\mathbf{x}) - \varepsilon_{\mathrm{b}}) + (\sigma^{\mathrm{r}}(\mathbf{x}) + \sigma_{\mathrm{b}})\big)\,\mathrm{d}V \\ &+ \iiint_{\mathbf{x}\in\mathcal{K}} \hat{\underline{\mathbf{G}}}^{\mathbf{HK}}(\mathbf{x}', \mathbf{x}, \mathrm{j}\omega)\hat{\mathbf{K}}^{\mathrm{r}}(\mathbf{x})\,\mathrm{d}V, \quad \text{for } \mathbf{x}' \in \mathbb{R}^3,\end{aligned} \tag{3.3.28}$$

in which the domain $\mathcal{V}$ is the domain outside the human body and the domain $\mathcal{S}$ is the domain that contains the body that is acting as a transmitter. In equation Eq. (3.3.28) the first expression is the contribution due to the induced electric field in the body (and pads), that can be seen as an introduction of noise on the received magnetic field, and the second expression is due to the magnetic field in the exciting state that now is a magnetic source and is defined trough Eq. (3.3.17)

Chapter 4

Simplified pad model

In this chapter we study some properties of the high permittivity pads. We first study the influence of the conductivity of a pad on the spatial variation of the B_1^+ field. We show that lossless pads have the best performance and produce the smallest spatial variations in the B_1^+ field. Second, the influence of the geometry of an object is studied. Sled and Pike [23] have shown that the field distribution is greatly affected by the shape of the object under test. To obtain a better understanding of these geometrical effects, we use a phantom model and study the field patterns for different phantom shapes. Finally, the field patterns of the dielectric pads are studied and we demonstrate that the fields induced by the pads can be described using the so-called thin-sheet approximation.

4.1 Conductivity effects

To investigate how the conductivity of a pad influences the homogeneity of the B_1^+ field, we consider the experimental setup shown in Fig. 4.1. A birdcage operates at a frequency of $f = 128$ MHz and is loaded with a phantom model and high permittivity pads located symmetrically on either side of the phantom. The relative permittivity of the phantom is $\varepsilon_\mathrm{r} = 63.5$ and a conductivity of $\sigma = 0.72$ which are the material properties of muscle. The pads have a relative permittivity $\varepsilon_{\mathrm{r;pad}} = 300$. We use the so-called coefficient of variation

$$C_v = \frac{\text{Standard Deviation}}{\text{Mean}} \tag{4.1.1}$$

as a measure for the spatial variation of the B_1^+ field.

Figure 4.1: Birdcage coil with a phantom, with the tissue properties of muscle, as a load. Two pads (blue and green) are placed on both sides of the phantom and can be varied in conductivity.

In our first set of experiments, we take three different values for the conductivity of the pads, namely, $\sigma = 0.01$ S/m, $\sigma = 0.26$ S/m, and $\sigma = 0.56$ S/m. The magnitude of the corresponding B_1^+ fields is shown in Fig. 4.2. As can be seen from the figure, the conductivity has a dramatic influence on the homogeneity of the B_1^+ field. We observe that the inhomogeneity of the B_1^+ field increases with the conductivity of the pads.

To investigate this issue further, we carried out a parameter sweep and computed the coefficient of variation for pad conductivity values ranging from $\sigma = 0.001$ S/m to $\sigma = 0.56$ S/m. Fig. 4.3 shows the result of this experiment.

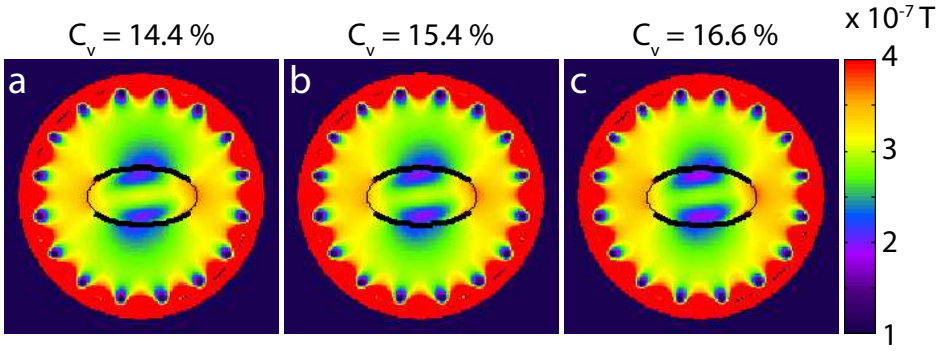

Figure 4.2: B_1^+ maps three different conductivity values for the pads. In figure a the conductivity is 0.01 (S/m), in figure b the coductivity is 0.26 (S/m) and for figure c a conductivity of 0.56 (S/m) is chosen

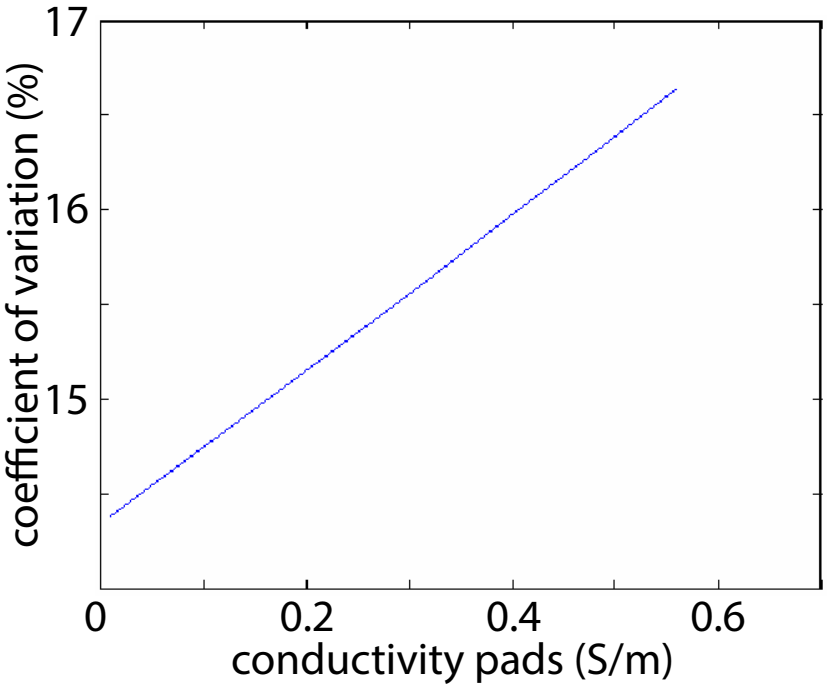

Figure 4.3: Conductivity grid search with the corresponding coefficients of variation

Surprisingly, the coefficient of variation depends linearly on the conductivity

of the pads and increases for increasing conductivity values. From these results we conclude that the best performance is obtained with low conductivity or lossless pads. [1]

4.2 Shape Differences

In [23], it is demonstrated that the shape of an object can have a large influence on the B_1^+ field distribution. Let us verify this claim by gradually changing the shape of the phantom model. The medium parameters of the phantom are again equal to the tissue parameters of muscle at 128 MHz. The various phantom shapes (ranging from elliptical to spherical) are shown in Figs. 4.4 and 4.5 along with the corresponding magnitudes of the B_1^+ field and the electric field strength. From these figures, we observe that the fields indeed do change significantly if the shape of the phantom is changed. Comparing the coefficient of variation within the different phantoms, we observe that the phantom with a circular cross section is not the most optimal one as might be expected. The B_1^+ field exhibits strong inhomogeneities inside the circular phantom leading to a relatively large coefficient of variation.

[1] For completeness, we mention that we arrived at similar conclusions by solving a simple one-dimensional multi-layer problem using a Matlab code provided by Rob Remis.

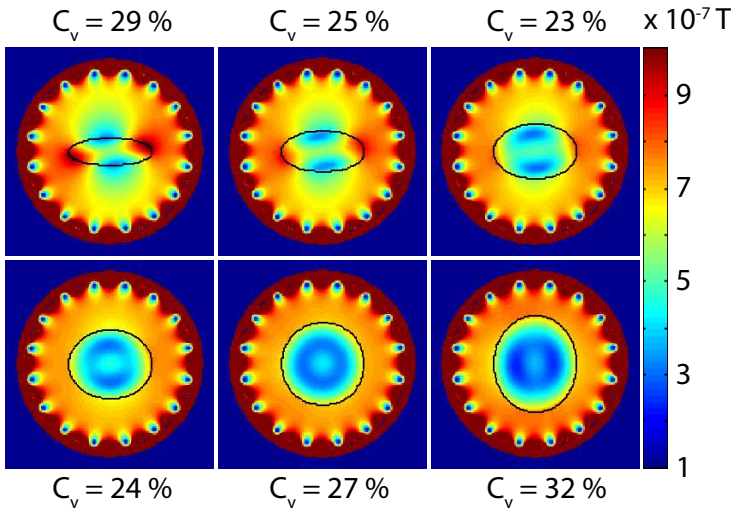

Figure 4.4: The B_1^+ field in the z-direction for varying shapes (roundness) of the phantom with the tisue properties of muscle

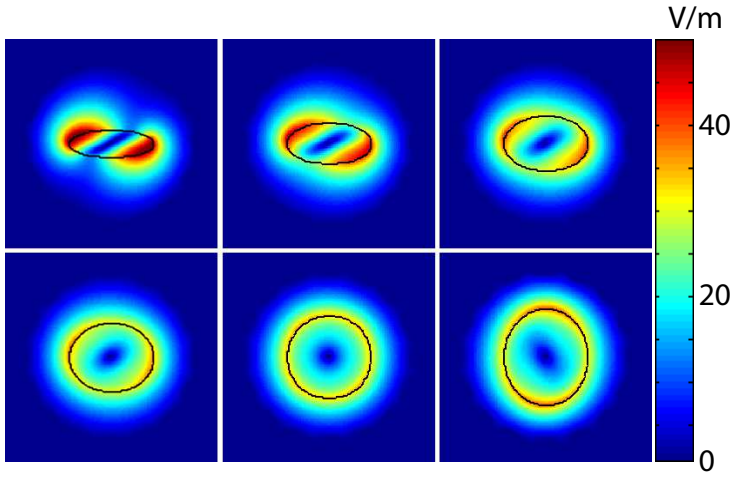

Figure 4.5: The electric field in the z-direction for varying shapes (roundness) of the phantom with the tisue properties of muscle

From these result it can be concluded that the shape (roundness) of an object has a big impact as mentions earlier by [23]. Further it is interesting to note that a perfect circular object does not have the greatest homogeneity in the B_1^+ field.

4.3 Scattering formalism for a phantom-pad model

In this section, we study the structure of the electromagnetic field as generated by a so-called birdcage. The birdcage occupies the source domain $\mathbb{D}^{\text{src}}$ and is loaded with a phantom and dielectric pads (see Fig. 4.1). The phantom occupies the domain $\mathbb{D}^{\text{phan}}$ and is characterized by a position dependent conductivity $\sigma(\mathbf{x})$ and permittivity $\varepsilon(\mathbf{x})$. High-permittivity pads are placed on both sides of the phantom. The pads occupy the domain $\mathbb{D}^{\text{pad}}$ and the conductivity and permittivity of the pads are given by $\sigma^{\text{pad}}(\mathbf{x})$ and $\varepsilon^{\text{pad}}(\mathbf{x})$, respectively. The surrounding medium consists of air with a permittivity ε_0. The complete configuration shows no contrast in the permeability and therefore $\mu = \mu_0$ everywhere. To describe the electromagnetic wave field inside this configuration, we make use of the linearity of Maxwell's equations and setup a scattering formalism. In particular, we write the electromagnetic field as a superposition of a field that would be present if the phantom was absent, and a field that takes the presence of the phantom into account. We refer to the former field as the background field and denote it by $\{\hat{\mathbf{E}}^{\text{b}}(\mathbf{x}, \mathrm{j}\omega), \hat{\mathbf{H}}^{\text{b}}(\mathbf{x}, \mathrm{j}\omega)\}$, while the latter field is called the scattered field and is denoted by $\{\hat{\mathbf{E}}^{\text{phan}}(\mathbf{x}, \mathrm{j}\omega), \hat{\mathbf{H}}^{\text{phan}}(\mathbf{x}, \mathrm{j}\omega)\}$. To summarize, the total field in our configuration is written as

$$\{\hat{\mathbf{E}}, \hat{\mathbf{H}}\} = \{\hat{\mathbf{E}}^{\text{b}} + \hat{\mathbf{E}}^{\text{phan}}, \hat{\mathbf{H}}^{\text{b}} + \hat{\mathbf{H}}^{\text{phan}}\}, \tag{4.3.1}$$

and in this section we discuss the equations that are satisfied by these fields.

Let us start with the background field. Introducing the background conductivity and permittivity as

$$\sigma_{\text{b}}(\mathbf{x}) = \begin{cases} 0 & \text{for } \mathbf{x} \notin \mathbb{D}^{\text{pad}}, \\ \sigma^{\text{pad}}(\mathbf{x}) & \text{for } \mathbf{x} \in \mathbb{D}^{\text{pad}}, \end{cases} \tag{4.3.2}$$

and

$$\varepsilon_{\text{b}}(\mathbf{x}) = \begin{cases} \varepsilon_0 & \text{for } \mathbf{x} \notin \mathbb{D}^{\text{pad}}, \\ \varepsilon^{\text{pad}}(\mathbf{x}) & \text{for } \mathbf{x} \in \mathbb{D}^{\text{pad}}, \end{cases} \tag{4.3.3}$$

respectively, the background field satisfies the equations

$$-\boldsymbol{\nabla} \times \hat{\mathbf{H}}^{\text{b}} + (\sigma_{\text{b}} + \mathrm{j}\omega\varepsilon_{\text{b}})\hat{\mathbf{E}}^{\text{b}} = -\hat{\mathbf{J}}^{\text{ext}}, \tag{4.3.4}$$

$$\boldsymbol{\nabla} \times \hat{\mathbf{E}}^{\text{b}} + \mathrm{j}\omega\mu_0\hat{\mathbf{H}}^{\text{b}} = \mathbf{0}, \tag{4.3.5}$$

for $\mathbf{x} \notin \mathbb{D}^{\text{phan}}$, and

$$-\boldsymbol{\nabla} \times \hat{\mathbf{H}}^{\text{b}} + (\sigma_{\text{b}} + \text{j}\omega\varepsilon_{\text{b}})\hat{\mathbf{E}}^{\text{b}} = \mathbf{0}, \tag{4.3.6}$$

$$\boldsymbol{\nabla} \times \hat{\mathbf{E}}^{\text{b}} + \text{j}\omega\mu_0\mathbf{H}^{\text{b}} = \mathbf{0}, \tag{4.3.7}$$

for $\mathbf{x} \in \mathbb{D}^{\text{phan}}$. Equations (4.3.4) – (4.3.7) govern the behaviour of the electromagnetic background field.

To take the presence of the phantom into account, we first consider the total electromagnetic field. This field satisfies

$$-\boldsymbol{\nabla} \times \hat{\mathbf{H}} + (\sigma_{\text{b}} + \text{j}\omega\varepsilon_{\text{b}})\hat{\mathbf{E}} = -\hat{\mathbf{J}}^{\text{ext}}, \tag{4.3.8}$$

$$\boldsymbol{\nabla} \times \hat{\mathbf{E}} + \text{j}\omega\mu_0\hat{\mathbf{H}} = \mathbf{0}, \tag{4.3.9}$$

for $\mathbf{x} \notin \mathbb{D}^{\text{phan}}$, and

$$-\boldsymbol{\nabla} \times \hat{\mathbf{H}} + (\sigma + \text{j}\omega\varepsilon)\hat{\mathbf{E}} = \mathbf{0}, \tag{4.3.10}$$

$$\boldsymbol{\nabla} \times \hat{\mathbf{E}} + \text{j}\omega\mu_0\hat{\mathbf{H}} = \mathbf{0}, \tag{4.3.11}$$

for $\mathbf{x} \in \mathbb{D}^{\text{phan}}$. Rewriting Eq. (4.3.10) as

$$-\boldsymbol{\nabla} \times \hat{\mathbf{H}} + (\sigma_{\text{b}} + \text{j}\omega\varepsilon_{\text{b}})\hat{\mathbf{E}} = -[\sigma - \sigma_{\text{b}} + \text{j}\omega(\varepsilon - \varepsilon_{\text{b}})]\hat{\mathbf{E}}, \tag{4.3.12}$$

the equations for the total field inside the phantom can be written as

$$-\boldsymbol{\nabla} \times \hat{\mathbf{H}} + (\sigma_{\text{b}} + \text{j}\omega\varepsilon_{\text{b}})\hat{\mathbf{E}} = -[\sigma - \sigma_{\text{b}} + \text{j}\omega(\varepsilon - \varepsilon_{\text{b}})]\hat{\mathbf{E}}, \tag{4.3.13}$$

$$\boldsymbol{\nabla} \times \hat{\mathbf{E}} + \text{j}\omega\mu_0\hat{\mathbf{H}} = \mathbf{0}, \tag{4.3.14}$$

with $\mathbf{x} \in \mathbb{D}^{\text{phan}}$. Subtracting now Eqs. (4.3.4) and (4.3.5) from Eqs. (4.3.8) and (4.3.9), respectively, we obtain

$$-\boldsymbol{\nabla} \times \hat{\mathbf{H}}^{\text{phan}} + (\sigma_{\text{b}} + \text{j}\omega\varepsilon_{\text{b}})\hat{\mathbf{E}}^{\text{phan}} = \mathbf{0}, \tag{4.3.15}$$

$$\boldsymbol{\nabla} \times \hat{\mathbf{E}}^{\text{phan}} + \text{j}\omega\mu_0\hat{\mathbf{H}}^{\text{phan}} = \mathbf{0}, \tag{4.3.16}$$

for $\mathbf{x} \notin \mathbb{D}^{\text{phan}}$. Similarly, subtracting Eqs. (4.3.6) and (4.3.7) from Eqs. (4.3.13) and (4.3.14), respectively, results in

$$-\boldsymbol{\nabla} \times \hat{\mathbf{H}}^{\text{phan}} + (\sigma_{\text{b}} + \text{j}\omega\varepsilon_{\text{b}})\hat{\mathbf{E}}^{\text{phan}} = -[\sigma - \sigma_{\text{b}} + \text{j}\omega(\varepsilon - \varepsilon_{\text{b}})]\hat{\mathbf{E}}, \tag{4.3.17}$$

$$\boldsymbol{\nabla} \times \hat{\mathbf{E}}^{\text{phan}} + \text{j}\omega\mu_0\hat{\mathbf{H}}^{\text{phan}} = \mathbf{0}, \tag{4.3.18}$$

with $\mathbf{x} \in \mathbb{D}^{\text{phan}}$. Introducing the scattering source $\hat{\mathbf{J}}^{\text{phan}}$ as

$$\hat{\mathbf{J}}^{\text{phan}}(\mathbf{x}) = \begin{cases} \mathbf{0} & \text{for } \mathbf{x} \notin \mathbb{D}^{\text{phan}}, \\ [\sigma - \sigma_{\text{b}} + \mathrm{j}\omega(\varepsilon - \varepsilon_{\text{b}})]\hat{\mathbf{E}} & \text{for } \mathbf{x} \in \mathbb{D}^{\text{phan}}, \end{cases} \tag{4.3.19}$$

we can write Eqs. (4.3.15) – (4.3.18) more compactly as

$$-\boldsymbol{\nabla} \times \hat{\mathbf{H}}^{\text{phan}} + (\sigma_{\text{b}} + \mathrm{j}\omega\varepsilon_{\text{b}})\hat{\mathbf{E}}^{\text{phan}} = -\hat{\mathbf{J}}^{\text{phan}}, \tag{4.3.20}$$

$$\boldsymbol{\nabla} \times \hat{\mathbf{E}}^{\text{phan}} + \mathrm{j}\omega\mu_0\hat{\mathbf{H}}^{\text{phan}} = \mathbf{0}, \tag{4.3.21}$$

for $\mathbf{x} \in \mathbb{R}^3$. These are the equations for the scattered field.

To summarize, the equations for the background field $\{\hat{\mathbf{E}}^{\text{b}}, \hat{\mathbf{H}}^{\text{b}}\}$ are

$$-\boldsymbol{\nabla} \times \hat{\mathbf{H}}^{\text{b}} + (\sigma_{\text{b}} + \mathrm{j}\omega\varepsilon_{\text{b}})\hat{\mathbf{E}}^{\text{b}} = -\hat{\mathbf{J}}^{\text{ext}}, \tag{4.3.22}$$

$$\boldsymbol{\nabla} \times \hat{\mathbf{E}}^{\text{b}} + \mathrm{j}\omega\mu_0\hat{\mathbf{H}}^{\text{b}} = \mathbf{0}, \tag{4.3.23}$$

$\mathbf{x} \in \mathbb{R}^3$, while the equations for the scattered field $\{\hat{\mathbf{E}}^{\text{phan}}, \hat{\mathbf{H}}^{\text{phan}}\}$ are

$$-\boldsymbol{\nabla} \times \hat{\mathbf{H}}^{\text{phan}} + (\sigma_{\text{b}} + \mathrm{j}\omega\varepsilon_{\text{b}})\hat{\mathbf{E}}^{\text{phan}} = -\hat{\mathbf{J}}^{\text{phan}}, \tag{4.3.24}$$

$$\boldsymbol{\nabla} \times \hat{\mathbf{E}}^{\text{phan}} + \mathrm{j}\omega\mu_0\hat{\mathbf{H}}^{\text{phan}} = \mathbf{0}, \tag{4.3.25}$$

for $\mathbf{x} \in \mathbb{R}^3$.

The Background Electromagnetic Field

To get some insight into the behaviour of the background electromagnetic field, we again follow a scattering formalism. Recall that the background field is the field with dielectric pads included, but in absence of the human phantom. This field satisfies Eqs. (4.3.22) and (4.3.23).

Now let the incident field be the field that is present if the birdcage is empty. We denote this field by $\{\hat{\mathbf{E}}^{\text{i}}, \hat{\mathbf{H}}^{\text{i}}\}$ and it satisfies the equations

$$-\boldsymbol{\nabla} \times \hat{\mathbf{H}}^{\text{i}} + \mathrm{j}\omega\varepsilon_0\hat{\mathbf{E}}^{\text{i}} = -\hat{\mathbf{J}}^{\text{ext}}, \tag{4.3.26}$$

$$\boldsymbol{\nabla} \times \hat{\mathbf{E}}^{\text{i}} + \mathrm{j}\omega\mu_0\hat{\mathbf{H}}^{\text{i}} = \mathbf{0}, \tag{4.3.27}$$

for $\mathbf{x} \in \mathbb{R}^3$. Introducing the scattered field due to the presence of the pad as

$$\{\hat{\mathbf{E}}^{\text{sc}}, \hat{\mathbf{H}}^{\text{sc}}\} = \{\hat{\mathbf{E}}^{\text{b}} - \hat{\mathbf{E}}^{\text{i}}, \hat{\mathbf{H}}^{\text{b}} - \hat{\mathbf{H}}^{\text{i}}\}, \tag{4.3.28}$$

and following a similar procedure as above, we find that the scattered field satisfies the equations

$$-\boldsymbol{\nabla} \times \hat{\mathbf{H}}^{\mathrm{sc}} + \mathrm{j}\omega\varepsilon_0 \hat{\mathbf{E}}^{\mathrm{sc}} = -\hat{\mathbf{J}}^{\mathrm{sc}}, \tag{4.3.29}$$

$$\boldsymbol{\nabla} \times \hat{\mathbf{E}}^{\mathrm{sc}} + \mathrm{j}\omega\mu_0 \hat{\mathbf{H}}^{\mathrm{sc}} = \mathbf{0}, \tag{4.3.30}$$

for $\mathbf{x} \in \mathbb{R}^3$, where we have introduced the scattering source due to the pad as

$$\hat{\mathbf{J}}^{\mathrm{sc}}(\mathbf{x}) = \begin{cases} \mathbf{0} & \text{if } \mathbf{x} \notin \mathbb{D}^{\mathrm{pad}}, \\ [\sigma^{\mathrm{pad}} + \mathrm{j}\omega(\varepsilon^{\mathrm{pad}} - \varepsilon_0)]\hat{\mathbf{E}}^{\mathrm{b}} & \text{if } \mathbf{x} \in \mathbb{D}^{\mathrm{pad}}. \end{cases} \tag{4.3.31}$$

With this result, we have all the basic equations available and all the different electromagnetic fields can be in principle be determined.

4.3.1 The simulated incident field

To identify the contributions from the various fields defined in the previous section, let us start with the incident field $\{\hat{\mathbf{E}}^{\mathrm{i}}, \hat{\mathbf{H}}^{\mathrm{i}}\}$ that is present when the birdcage is unloaded. The birdcage operates at a frequency of $f = 128$ MHz and simulations were carried out using FDTD. Figures 4.6 (a) and (b) show the magnitude of the B_1^+ field and electric field strength, respectively. We observe that the B_1^+ field is very homogeneous when the birdcage is unloaded. The magnitude of the electric field strength has a zero in the middle of the coil because all the contributions of the individual birdcage rungs cancel each other out.

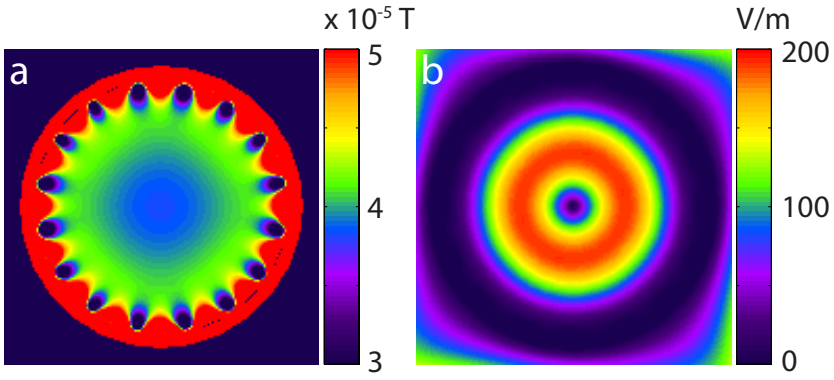

Figure 4.6: Empty birdcage coil at a frequency of 128 MHz. Magnitude of the B_1^+ field (a) and magnitude of the z-component of the electric field strength (b).

4.3.2 The simulated background field

Let us now load the birdcage with two dielectric pads. The pads are homogeneous and are taken to be lossless. The location of the pads is indicated in Fig. 4.1. The resulting electromagnetic field is the background field and in Fig. 4.7 we show the magnitude of certain components of this field. In particular, in Fig. 4.7 (c) the magnitude of the z-component of the electric field strength is shown, while the magnitude of the x- and y-components of the magnetic field strength are shown in Figs. 4.7 (a) and (b). From these figures, we observe that H_x^{b} shows an approximate odd symmetry across the pad, while E_z^{b} and H_y^{b} show an even symmetry. These symmetry properties can be explained using the so-called thin-sheet approximation [24]. Loosely speaking, this approximation can be applied if the scattering object is thin (compared with the wavelength) and its medium parameters are large. The pad obviously satisfies these requirements.

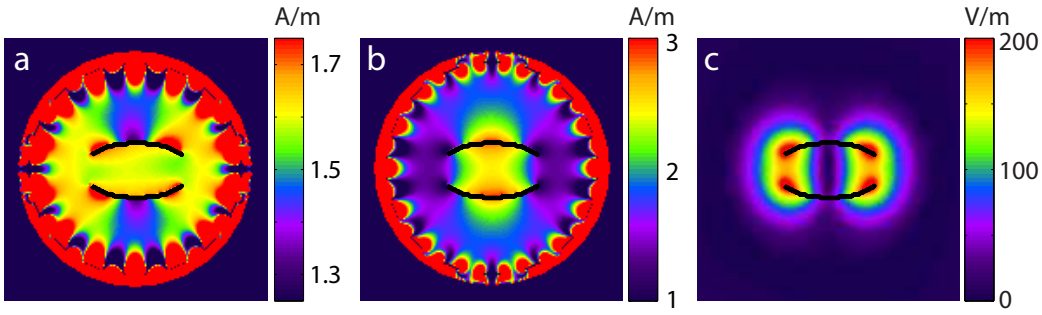

Figure 4.7: Field magnitudes for the birdcage with pads but without the phantom. Magnitude of the magnetic field in the x-direction (a), magnitude of the magnetic field in the y-direction (b), and magnitude of the electric field in the z-direction (c).

To be more precise, consider the pad shown in Fig. 4.8 which occupies the domain $\mathbb{D}^{\mathrm{pad}} = \{(x, z) \in \mathbb{A}, -a/2 < y < a/2\}$, where a is the thickness of the pad and $\mathbb{A} \subset \mathbb{R}^2$. The pad is assumed to be lossless and homogeneous and has a constant permittivity $\varepsilon_{\mathrm{pad}}$. For such a pad, the thin-sheet boundary conditions for the scattered field are [25]

$$\mathbf{i}_y \times \hat{\mathbf{E}}^{\mathrm{sc}}(x, a/2, z, \mathrm{j}\omega) - \mathbf{i}_y \times \hat{\mathbf{E}}^{\mathrm{sc}}(x, -a/2, z, \mathrm{j}\omega) = \mathcal{O}(a) \tag{4.3.32}$$

and

$$\mathbf{i}_y \times \hat{\mathbf{H}}^{\mathrm{sc}}(x, a/2, z, \mathrm{j}\omega) - \mathbf{i}_y \times \hat{\mathbf{H}}^{\mathrm{sc}}(x, -a/2, z, \mathrm{j}\omega) = \hat{\mathbf{J}}_{\mathrm{pad}} + \mathcal{O}(a), \quad (4.3.33)$$

for $(x, z) \in \mathbb{A}$ as $a \downarrow 0$. In the above equation,

$$\hat{\mathbf{J}}_{\mathrm{pad}} = \mathrm{j}\omega C_{\mathrm{pad}} \hat{\mathbf{E}}^{\mathrm{b}}(x, 0, z, \mathrm{j}\omega) \quad (4.3.34)$$

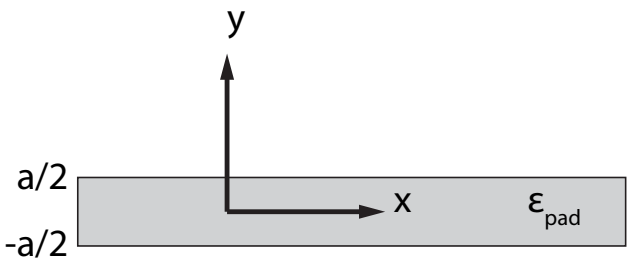

Figure 4.8: Pad with a thickness a, in the domain $\mathbb{D}^{\mathrm{pad}}$.

is the induced current inside the pad, where $C_{\mathrm{pad}} = \varepsilon_{\mathrm{pad}} a$. Taking the inner product of Eq. (4.3.33) with $\mathbf{i}_y$, we find $\mathbf{i}_y \cdot \hat{\mathbf{J}}_{\mathrm{pad}} = 0$ showing that there is no induced current in the y-direction. Consequently, we know that $\hat{E}_x^{\mathrm{sc}}$, $\hat{H}_y^{\mathrm{sc}}$, and $\hat{E}_z^{\mathrm{sc}}$ show even symmetry with respect to the plane $y = 0$, while $\hat{H}_x^{\mathrm{sc}}$, $\hat{E}_y^{\mathrm{sc}}$, and $\hat{H}_z^{\mathrm{sc}}$ are odd with respect to this plane [26]. The numerical results confirm this behaviour as can be seen from Figs. 4.7 (a), (b), and (c).

In Fig. 4.9 we show the magnitude of the B_1^+ field and the electric field strength. It is noticeable that the scale of the B_1^+ field has changed drastically. From the three situations it is clear that the relative permittivity $\varepsilon_{\mathrm{r;pad}}$ of the pad has a significant impact on the distribution of the field. This property can be used to shape the fields of a fully loaded birdcage (phantom and pads) and to obtain a homogeneous distribution of the B_1^+ field.

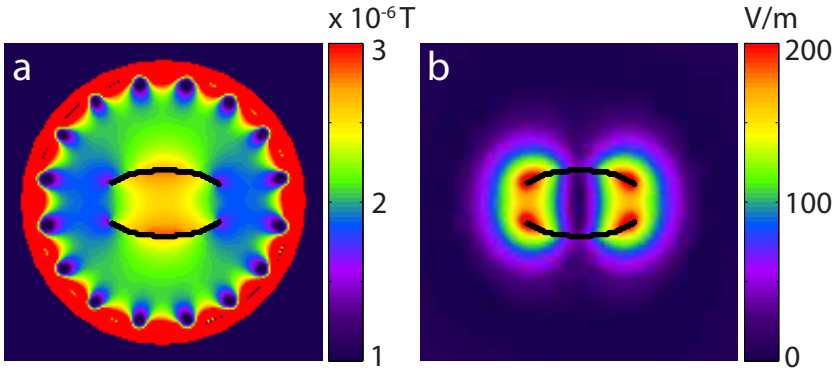

Figure 4.9: Birdcage coil with pads floating in free space. Magnitude of the B_1^+ field (a) and magnitude of the z-component of the electric field strength (b).

4.3.3 The simulated total field

In this final configuration, we consider a fully loaded birdcage with pads and phantom included. The magnitudes of the B_1^+ field and the z-component of the electric field are shown in Fig. 4.10. Clearly, the B_1^+ field changes drastically if a phantom is included. Furthermore, the electric field has changed in amplitude and distribution. The signal voids in the B_1^+ field at the front- and backside of the phantom should be countered.

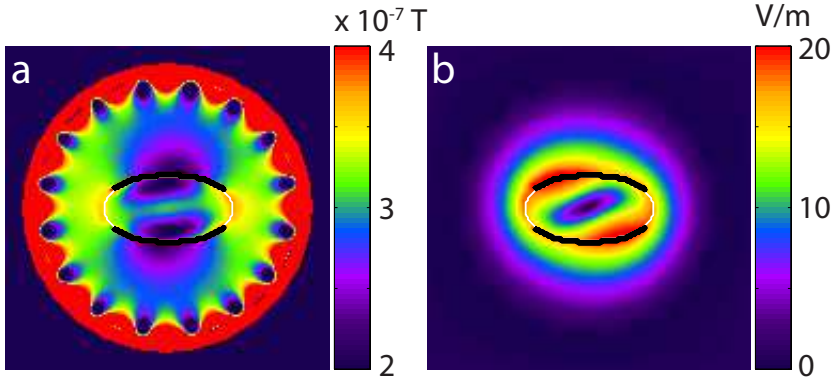

Figure 4.10: Birdcage coil with pads on top of the phantom. Magnitude of the B_1^+ field (a) and magnitude of the z-component of the electric field strength (b).

Finally, the same field components as in the previous subsection were computed to see how the field patterns get perturbed if the phantom is included. The magnitude of the relevant field components are shown in Fig. 4.7. We observe that due to the coupling between the pads and the phantom, the field patterns have been perturbed in such a way that the odd/even symmetry is less pronounced.

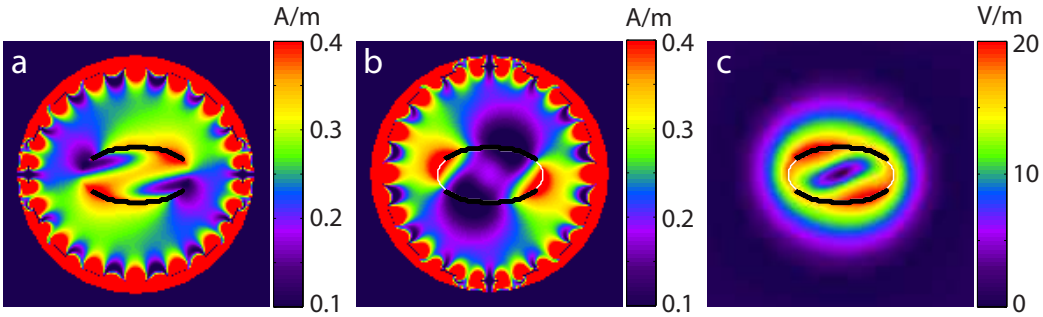

Figure 4.11: Birdcage coil with pads on top of the phantom. Magnitude of the magnetic field in the x-direction (a), magnitude of the magnetic field in the y-direction (b), and magnitude of the electric field in the z-direction (c).

Chapter 5

Numerical simulations and results

Chapters 5, 6 and 7 are published in [1]

Having studied the pad properties and pad behaviour in different scenarios, we now design pads for two realistic models (one male and one female) and demonstrate their performance. We carried out many different simulations to optimize the placement and material properties of the pads. This chapter gives a description of these simulations.

5.1 Electromagnetic simulations

A commercial package based on a Finite Difference Time Domain method (xFDTD, Remcom, PA) was used for all simulations. The RF coil was modelled as a 16 rung high pass birdcage coil with a diameter of 61 cm, length 56 cm, driven in quadrature mode by 32 ideal current sources with an impedance of 50 Ω. In Fig. 5.1 the birdcage coil is shown.

[1] *Increasing signal homogeneity and image quality in abdominal imaging at 3 T with very high permittivity materials*; de Heer P, Brink WM, Kooij BJ, Webb AG; Magnetic Resonance in Medicine, July 2012; DOI 10.1002/mrm.24438.

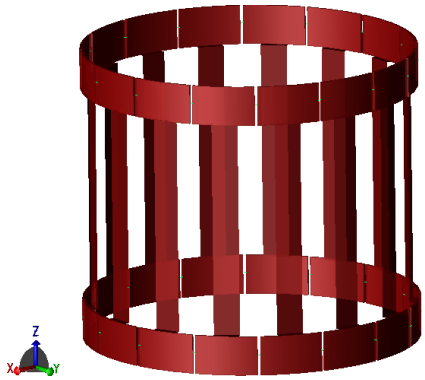

Figure 5.1: Bird cage coil tuned at the Larmor frequency for 3T field strength (128 MHz)

This corresponds to a dual transmit system being operated in the conventional quadrature or fixed phase mode, in which the phase relationship between the two channels is fixed at 90. One male (Duke, body mass index 23) or one female (Ella, body mass index 22) model from the virtual family [27] was placed in the center of the coil. An isotropic grid cell size of 2.5 mm was used with a seven-layer perfectly matched absorbing boundary. A sinusoidal current was applied at 128 MHz, with a time=step of 4.8 ps. A criterion of 50 dB was set for convergence of the steady-state fields, and typical simulation times were 30 min using a graphics processing unit. The transmit magnetic field (B_1^+), electric (E) field, and Specific Absorption Rate (SAR) were simulated for each configuration: normalization was set to 1 W dissipated power in tissue. To determine the optimal pad permittivity, a grid search was used in which the relative permittivity values of two pads (one anterior, one posterior), each of thickness 1 cm, were varied from 1 to 650 in steps of 50. For comparison, a 3-cm thick commercially available water pad [13] and [14] was included in the simulations. The coefficient of variation (C_v), defined in Chapter 4, of the B_1^+ field across the simulated B_1^+ map (transverse orientation) was evaluated in MATLAB (Mathworks, Natick, MA). In the transverse slices, the value of C_v is calculated throughout the entire cross-section (not considering the arms). For coronal slices, a rectangular region of interest is assigned through the thorax and abdominal region of the body.

Fig. 5.2 shows a schematic of the simulation set-up with bags on both the anterior as well as the posterior side of the model.

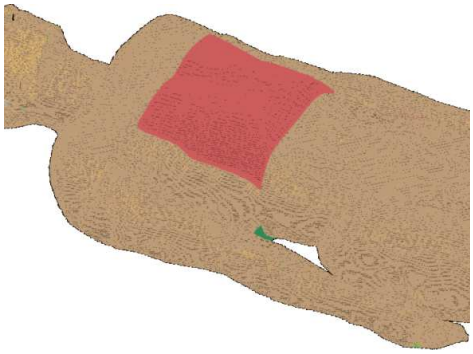

Figure 5.2: Schematic of the setup for the electromagnetic simulations with a dielectric pad (red) with thickness 1 cm placed on the abdomen. A identically shaped pad (green) is placed on the back, in the same position.

Fig. 5.3 shows simulation results of the B_1^+ field in the male Duke model. The grid search gave an optimum configuration with relative permittivities of 400 for the anterior pad and 500 for the posterior pad for a pad thickness of 1 cm. In practice, the highest permittivity that could be achieved was 300 using essentially a saturated suspension of barium titanate powder in water. In Fig 5.3, the values of C_v are given for the situations of no pads, the commercial pad (3-cm thick, water-based, $\varepsilon_r = 80$), the optimum configuration of the two pads placed anterior and posterior, and the practical configuration of two pads with relative permittivities of 300. As mentioned above, in the transverse slice, the value of C_v is calculated throughout the entire cross-section (not considering the arms), and for the coronal slice through the thorax and abdominal region of the body. There are considerable improvements in the B_1^+ homogeneity for the anterior/posterior high permittivity pads compared to both the situation with no pads, and also the asymmetric placement of the commercial pad on only the anterior side of the subject. It should be noted that, since optimization was performed on the transverse slice due to the much more defined region-of-interest (essentially the entire slice without the arms), the value of C_v in the coronal plane can actually be slightly lower for the $\varepsilon_r = 300$ case than the "optimum" permittivity value case.

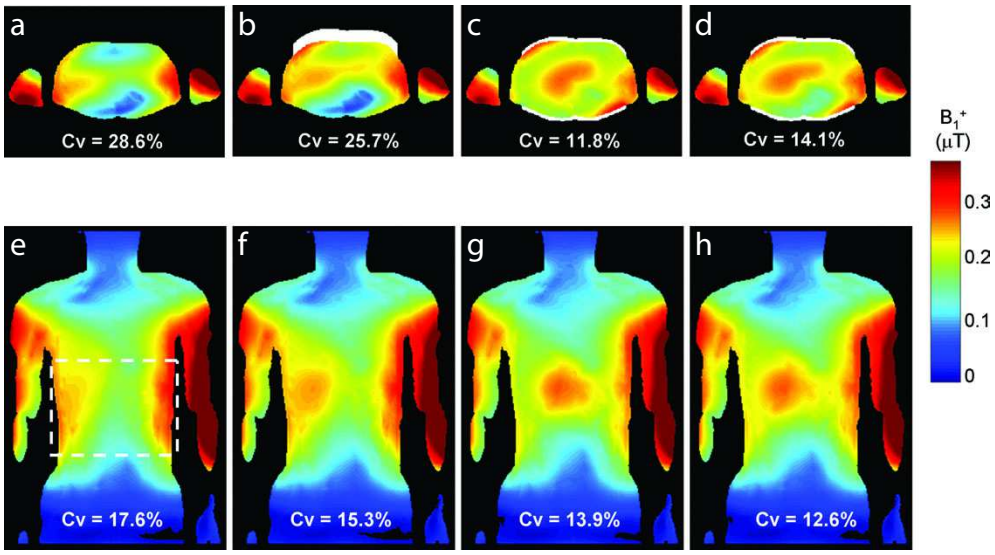

Figure 5.3: Electromagnetic simulations of the B_1^+ field in the "Duke" model. (a) – (d) transverse slice through the centre of the liver, (e) – (h) corresponding coronal slices. (a) and (e) no dielectric pads, (b) and (f) a 3 cm thick "commercial" water-based pad, (c) and (g) the optimum solution for two 1 cm thick pads with $\varepsilon_r = 400$ for the anterior pad and $\varepsilon_r = 500$ for the posterior pad, (d) and (h) the practically realizable situation with two 1 cm pads each with $\varepsilon_r = 300$. The coefficient of variation is shown for each configuration.

Fig. 5.4 shows corresponding plots for the female Ella model. In this case, the optimum configuration was found to correspond to relative permittivities of 300 for the front and back.

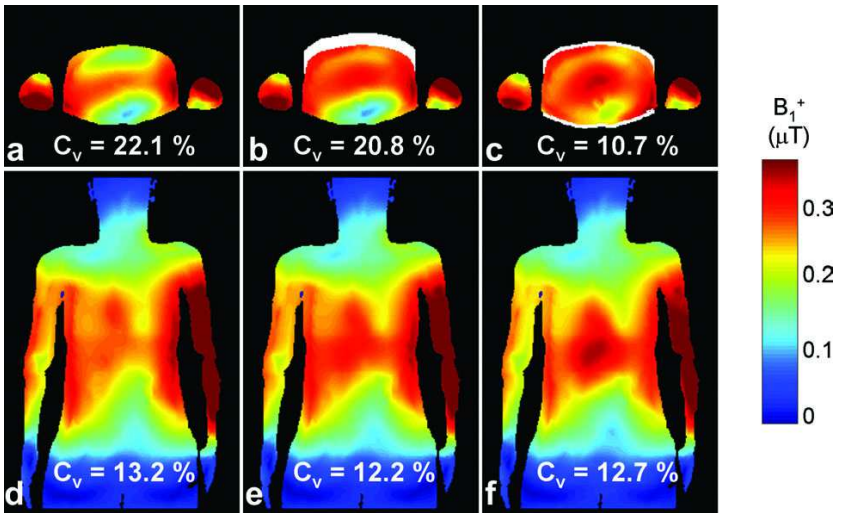

Figure 5.4: Electromagnetic simulations of the B_1^+ field in the "Ella" model. (a) – (c) transverse slice through the centre of the liver, (d) – (f) corresponding coronal slices. (a) and (d) no dielectric pads, (b) and (e) a 3 cm thick "commercial" water-based pad, (c) and (f) the optimum solution for two 1 cm thick pads with $\varepsilon_r = 300$ for the anterior pad and $\varepsilon_r = 300$ for the posterior pad.

The dependence of the value of C_v on the permittivities of the two pads for both the Duke and Ella model is shown in Fig. 5.5. As can be seen, there is a relatively smooth minimum for values around 300 – 500, but the increase is quite severe for values below about 300 or above 500. These results confirm the simulation results in Fig. 5.3 which demonstrate that there is a very small increase in C_v when operating with pads with permittivity of 300 compared to the optimum values of 400/500.

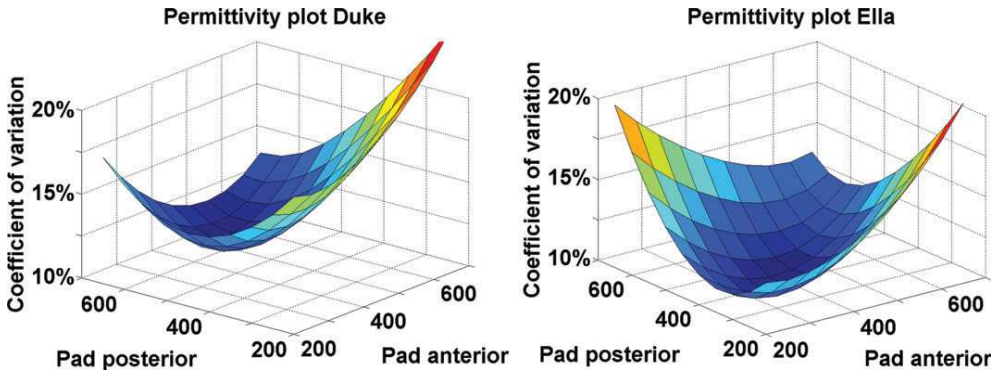

Figure 5.5: Plots of coefficient of variation (vertical axis) vs. the permittivities of both the anterior and posterior pads. (left) Duke and (right) Ella model.

To determine whether the high permittivity pads increase either the local or global SAR values, Fig. 5.6 shows transverse and coronal plots of the local (1 g tissue average) SAR values for the Duke model generated by the quadrature-driven body coil. The highest values are generally found in the arms (since they are in the region of the highest electric field of the RF coil), and all values in the body are at least a factor-of-two lower. There are negligible differences introduced by either the commercial or new high permittivity pads. Very similar results were found for Ella (data not shown). These results correspond to the conventional quadrature-driven body coil, but it is anticipated that similar effects occur in the RF-shimmed case.

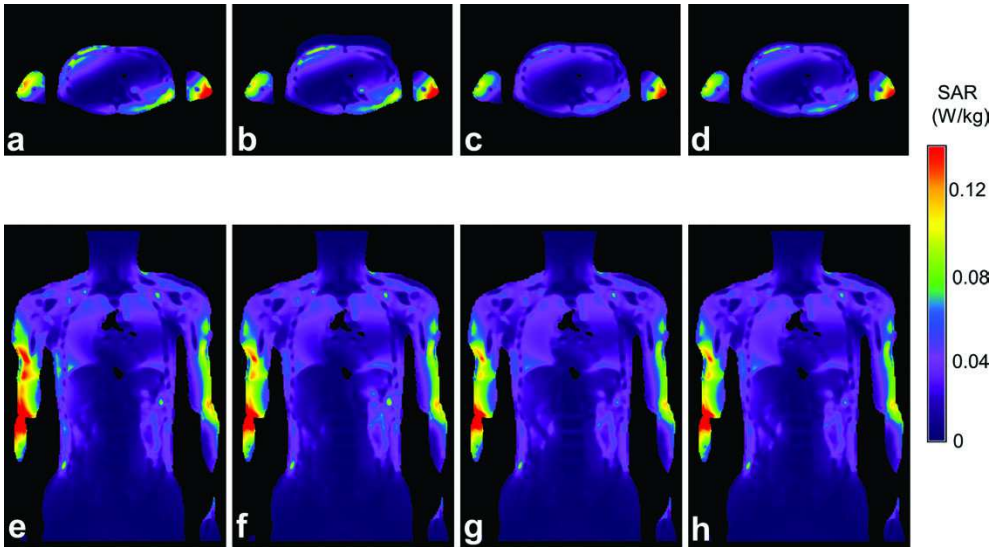

Figure 5.6: Electromagnetic simulations of the 1-g averaged SAR in the "Duke" model. (a)–(d) transverse slice through the centre of the liver, (e)–(h) corresponding coronal slices. (a) and (e) no dielectric pads, (b) and (f) a 3 cm thick "commercial" water-based pad, (c) and (g) the optimum solution for two 1 cm thick pads with $\varepsilon_r = 400$ for the anterior pad and $\varepsilon_r = 500$ for the posterior pad, (d) and (h) the practically realizable situation with two 1 cm pads each with $\varepsilon_r = 300$.

5.1.1 The polarization effect

The reason for the B_1^+ low signal intensities can be found in several properties like the amplitude of the field or the polarization of the field. To get the maximum signal we want a high amplitude and a circular polarization. This happens when the tip of the $\mathbf{B}_1$ field vector traces out a circular locus in space. This is the case when the real and complex components of the B_1^+ have the same size and are shifted 90 degrees in phase. The polarization can

also be described as a single number with the formula given in [28]

$$\xi = \frac{|B_1^+|}{|B_1^+| + |B_1^-|} \tag{5.1.1}$$

where,

$$\begin{aligned} \xi &= 1, \text{ circular polarization} \\ \xi &= 0.5, \text{ linear polarization} \\ 1 > \xi &> 0.5, \text{ eliptical polarization} \\ 0.5 > \xi &> 0, \text{ eliptical anti-quad polarization} \end{aligned}$$

So in short we want all the signal in the B_1^+ and no signal in the B_1^- because this will make the signal less circular. This was also checked by measuring the B_1^- polarization of an empty birdcage and comparing that to the amplitude of the B_1^-. From this we could see that in the unloaded case the B_1^- is zero and the polarization perfectly circular.

When we look at the B_1^+ maps in Fig. 5.3 for the case with and without pads we can clearly see low signal intensity regions if the pads are absent. These signal intensities increase by applying the optimized pads. We therefore check the polarizations in these regions. Several points in this area of low signal intensity were selected and the polarization number was calculated. The result of these values have been plotted over the B_1^+ map and can be seen in Fig. 5.8.

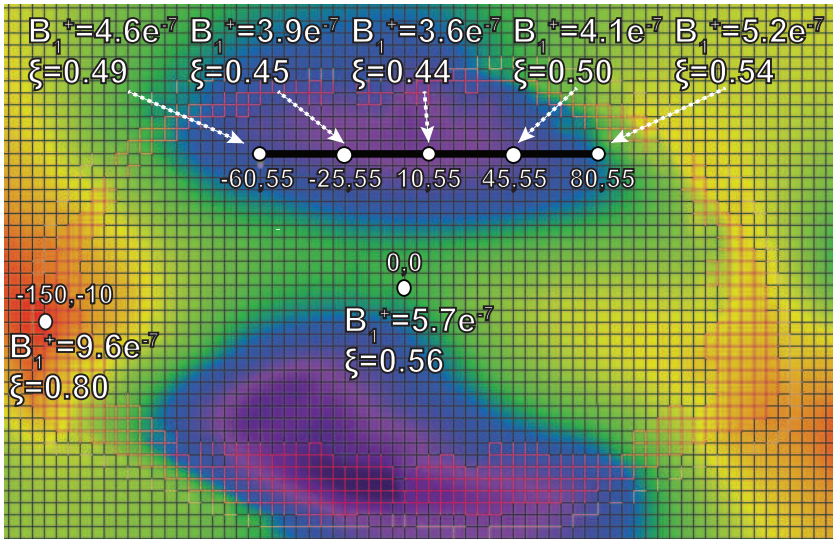

Figure 5.7: The B_1^+ map of Duke without pads. The low signal intensities can be seen at the anterior and posterior side of the torso. At the spot with low signal intensity anti-quad elliptical polarization is present.

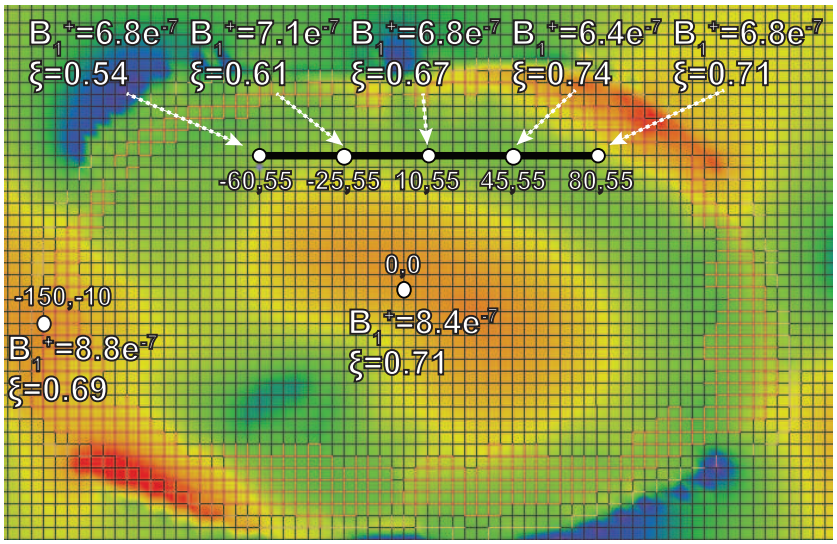

Figure 5.8: The B_1^+ map of Duke with optimized pads ($\varepsilon_{\mathrm{r;front}} = 450, \varepsilon_{\mathrm{r;back}} = 550$). The low signal intensities have been alleviated to create a much more homogeneous field distribution. The polarization has been changed more to an elliptical one.

From the images we can see that the case where no pads are used the polarization at the low spot is elliptical anti-quad polarization. When the pads are applied it is clear that at the location of low signal intensity the polarization goes to a more elliptical polarization and thus resulting in a higher B_1^+ amplitude at that location.

From this we can conclude that you can affect the polaration strongly by applying the pads. When the pads are well chosen the polarization will become more cirular, at the location of low signal intensity, and thus resulting in higher effective B_1^+.

Chapter 6

In-Vivo results

After the successful simulations with the pads the goal is now to replicate and validate these results In-Vivo. This was done with a Philips 3T scanner at the Leiden University Medical Center.

6.1 Production of high permittivity pads

High permittivity pads were produced based on the approach described previously [18]. Briefly, barium titanate (BaTiO3) powder (Alfa Aesar GmbH) was mixed with water until a saturated suspension was reached since the aim was to produce as high a permittivity as possible. Approximately, a 4:1 weight/weight ratio of barium titanate powder to water was used. The dielectric constant was measured using a dielectric probe kit (85070E, Agilent Technologies, Santa Clara, CA) and a network analyzer, and had a value of 300. This is substantially higher than reported in a previous publication [17], and emphasizes the fact that the permittivity that can be reached is critically dependent upon the surface properties and size of the barium titanate powder used. Two pads, each 1-cm thick, of the suspension were heat-sealed within polypropylene pads, with dimensions 28 x 22 cm^2 (left/right and head/foot dimensions, respectively). The weight of these pads was approximately 2 kg, significantly less both in thickness and weight compared to a commercial water-based pad (3 cm thick and 3.2 kg weight).

6.2 MRI protocols

All experiments were approved by the Leiden University Medical Center Committee for Medical Ethics, and performed on a dual-transmit 3 T Philips Achieva. Nine volunteers (seven male, two female), with ages between 25 and 50, and body mass indices (BMI's) between 18 and 38, were imaged. The transmit coil was the inbuilt body resonator, and a six-element "cardiac array" was used for signal reception: this consisted of three elements anterior and three elements posterior to the patient. All experiments were performed first with the pads in place, the pads were then removed with as little subject motion as possible, and rescanning without the pads was performed. Fig. 6.1 shows a schematic of the a photograph of the positioning of the thin pad on the anterior side of the volunteer.

Figure 6.1: Positioning of the thin pad on the anterior side of the volunteer.

The transmit field of the body coil was mapped using the method of Yarnykh [29] at 2.5 mm isotropic resolution with a target angle of 45° to avoid ambiguity for any actual tip angle close to or greater than 90°. Imaging parameters: three-dimensional gradient echo sequence: echo time = 20 ms, TR1 = 100 ms, TR2 = 250 ms, nominal flip angle 50, 64 x 64 data matrix, transverse slice thickness 10 mm, 1 mm slice gap, field-of-view 250 x 450 x 120 mm^3 with slight variations dependent upon subject size. Tip angle maps were generated from the ratio of the signal intensities obtained with the two different pulse repetition time values. Tip angle maps were then converted to transmit sensitivity (B_1^+ per square root of power) for direct comparison with EM simulations. Coefficient of variation values were calculated as described in the previous chapter. For assessment of image quality, T1-weighted turbo

gradient echo sequences were run with the following parameters: echo time = 2.3 ms, pulse repetition time = 10 ms, tip angle = 15°, 252 x 149 data matrix, slice thickness = 7 mm, 1 mm slice gap, field-of-view = 297 x 375 x 77, acquisition time = 13.5 s for six slices, linear phase encoding, scan percentage 75 %, turbo echo factor 149, no flow compensation. Images were acquired during breath-hold (exhalation). Four different settings were used to investigate the separate effects of RF shimming and the dielectric pads. First, RF shimming was turned off forcing the conventional quadrature relationship between the two separate transmit channels. Second, RF shimming was enabled, in which a rapid grid search is performed by the Philips system with a free range of relative amplitudes and phase difference between the two channels. RF shimming was performed separately for the cases with and without the dielectric pads in place. Measurements of the time-averaged power during the imaging sequence are recorded in the log file of the scanner. These measurements are performed directly at the amplifier, and measure both the forward and reflected powers, the difference between the two being the power delivered to the system (losses in cables and connectors between the RF amplifiers and the RF coil may be up to 15 %, but this percentage does not vary significantly with absolute power).

6.3 Experimental results

Fig. 6.2 shows transverse slices acquired for five of the nine volunteers (for clarity) for all four configurations of with/without RF shimming and with/without high permittivity pads. Clear improvements in image homogeneity are evident with the addition of the pads.

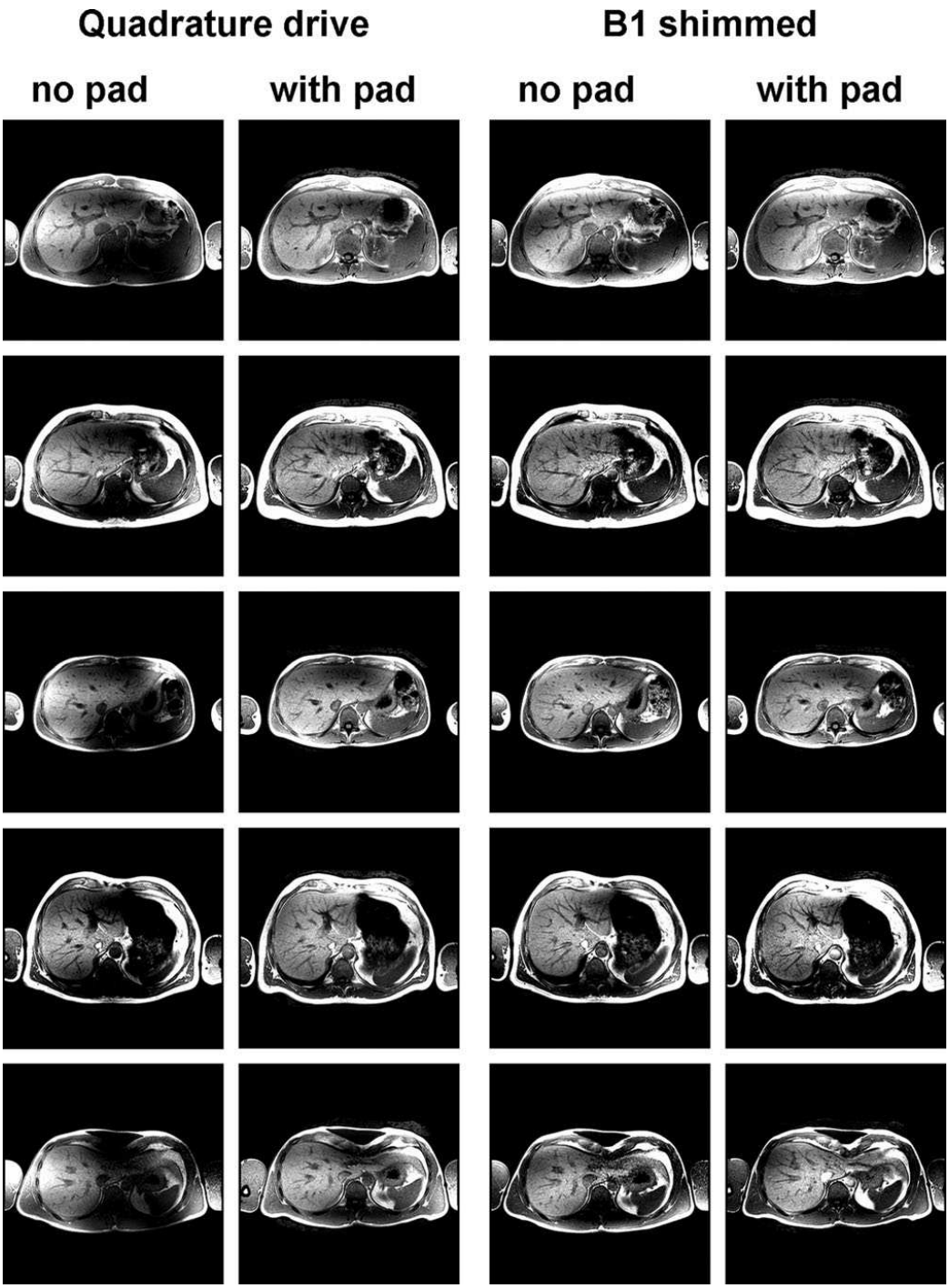

Figure 6.2: Comparison of T1-weighted turbo-spin echo images acquired from five volunteers with BMI values between 18 and 24 for four different configurations of quadrature/RF-shimmed drive and without/with dielectric pads.

Fig. 6.3 demonstrated the B_1^+ maps acquired without and with the dielectric pads in place for the same volunteers and the same conditions as shown in Fig. 6.2. From the figures it can be seen that there is good agreement with the simulated results presented in Fig. 5.3.

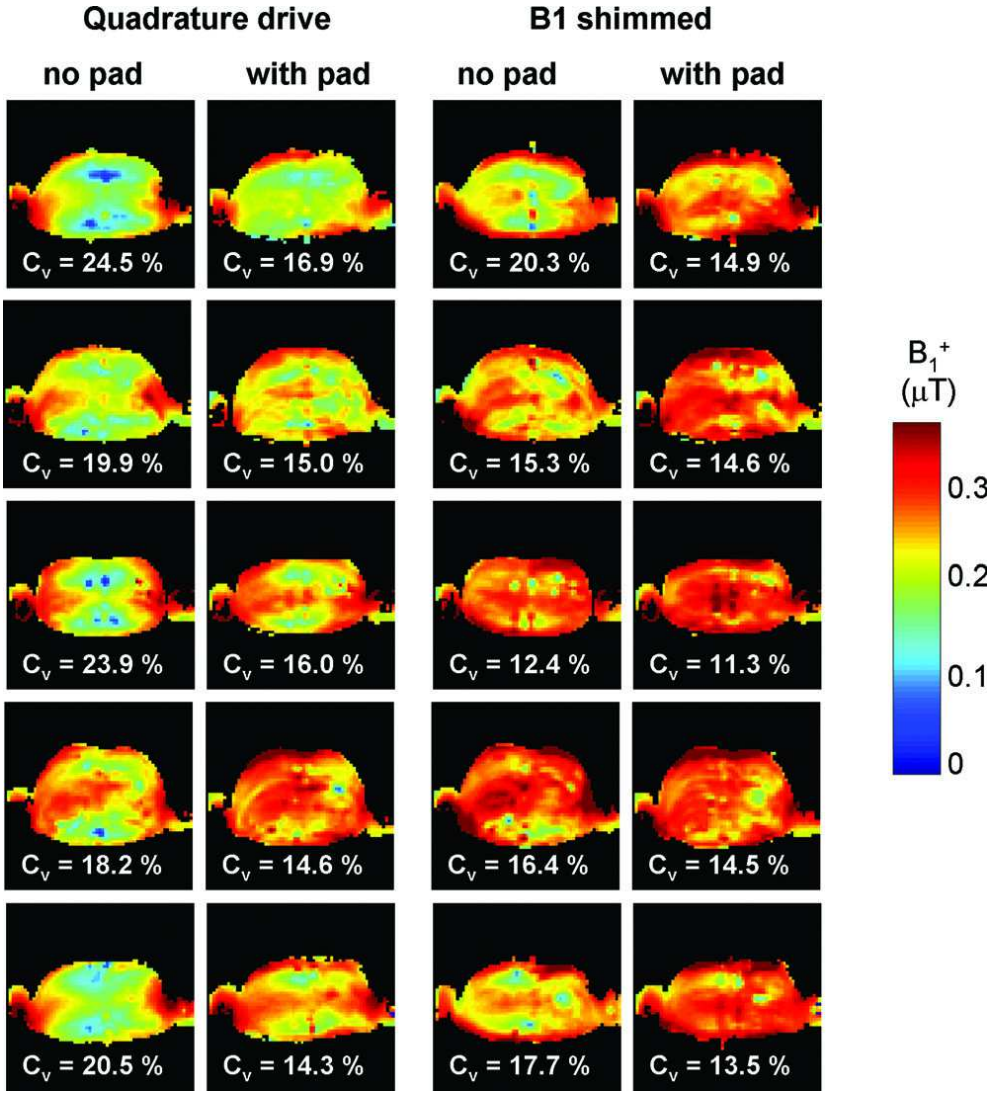

Figure 6.3: Measured B_1^+ maps from the same volunteers as in Fig. 6.2 for the same four configurations.

6.4 Statistical Analysis

Statistical analysis was performed using Graphpad Prism (La Jolla, CA). Paired two-sided Students t-tests were performed for conditions of with/without dielectric pads for data acquired with and without the dielectric pads. Fig. 6.4 shows a plot of the C_v for all nine volunteers for the four different imaging conditions. For the quadrature drive, the C_v decreased in all cases, and often by a substantial amount (mean $25.4 \pm 10\%$), with the addition of the dielectric pads. In the RF shimmed case, a decrease (mean $16 \pm 13\%$) in C_v for all but one case was achieved using the pads. Statistical analysis showed a significant decrease ($P < 0.0001$) in C_v between quadrature mode without and with the dielectric pads, and also in the RF shimmed case without and with the pads ($P = 0.005$).

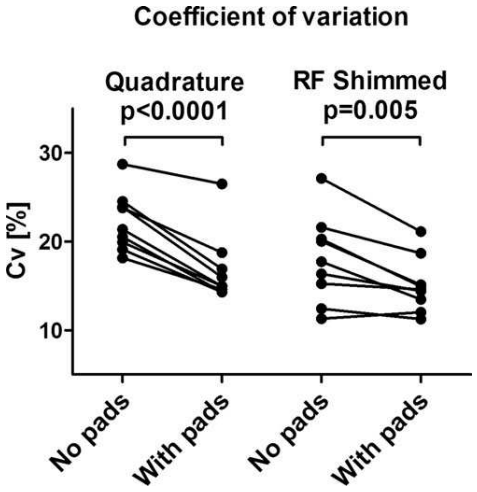

Figure 6.4: Plot of coefficient of variation for all nine volunteers. Statistically significant decreases are shown for both quadrature driven and RF-shimmed cases when introducing the dielectric pads.

In terms of the RF power required for image acquisition, there were also statistically significant reductions in both the peak power and time-averaged power using the dielectric pads. As with most power optimization algorithms on commercial systems, the average flip angle across the central transverse slice is calibrated. In the case of an inhomogeneous B_1^+ distribution, this causes overtipping in areas of high transmit efficiency, and undertipping in

areas of low efficiency. Fig. 6.5 shows the time-averaged power needed for the T1-weighted turbo gradient echo sequence used to produce the images in Fig. 6.2 these powers were read from the log file that was stored on the scanner, with the powers being measured at the output of the RF amplifier as described above. The power demands were in all but one case lower with pads than without pads. Statistical analysis showed a significant decrease in average power when the high permittivity pads were in place for both the quadrature-driven mode (P = 0.01) and RF shimmed mode (P = 0.0004).

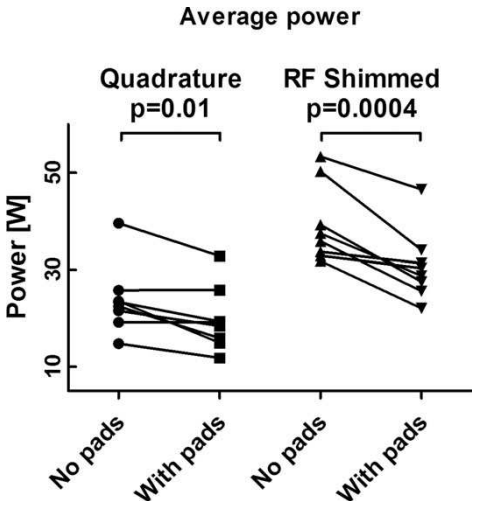

Figure 6.5: Plot of time averaged power measured for the images acquired in Fig. 6.2 for all nine volunteers. Statistically significant decreases are shown for both quadrature-driven and RF-shimmed cases when introducing the dielectric pads.

Chapter 7

Discussion and conclusion

The intrinsic inhomogeneity introduced by imaging an elliptical object with a quadrature RF coil is well known [23]. The recent commercial introduction of dual-transmit systems has shown substantial improvement in image quality, but does not yet represent a complete solution to the problem. This "solution" has also a big financial impact with prices of such a system ranging around $1.000.000.

7.1 Discussion

The ability of high permittivity materials [30] to increase the homogeneity of the transmit magnetic field has been shown primarily for neuroimaging at high field either with water bags [31] or materials formed from metal titanates [17, 18, 32]. Recently, improvements for neuroimaging at 3 T have also been reported using large water pads [33]. The lower the magnetic field, the higher the permittivity must be to compensate for B_1 inhomogeneities since displacement currents are proportional to the operating frequency. In the current work, we have demonstrated that statistically significant improvements in transmit efficiency (ratio between the power transmitted and the resulting effective magnetic field in the body) for abdominal imaging at 3 T can be achieved using thin, high permittivity pads placed anterior and posterior to the subject. The geometry which we studied, and where these results where acquired with, is relatively simple, consisting only of two pads of 1-cm thickness. It certainly can be anticipated that further improvements may result from optimized geometries including more pads in a more com-

plex geometry. Another refinement would be to optimize the coefficient of variance over the entire three-dimensional imaging volume, rather than just a central slice as in this work. Higher permittivity materials should bring further increases in image quality, as well as reduction in the thickness of the required pads, particularly in the case of patients with higher body mass index values than in healthy volunteers studied here. In this work no increases in global SAR (assuming body loss dominance) were evident, and indeed a reduction in local SAR was simulated for the quadrature-driven body coil. This was experimentally demonstrated by measuring substantial reductions in average power levels on the MR system both for the quadrature-driven mode, and also the RF-shimmed mode.

7.2 Conclusion

The proposed solution in this work, for homogenizing the transmit field in the body, allows to avoid the usage of expensive dual-transmit systems mentioned above while achieving similar results. When such a dual transmit system is available the image quality will still benefit by using the pads in combination with shimming.

The size of the rectangle pads was optimized and we can take as a rule of thumb that the pad should be as wide (left-right direction) as the area of low signal intensity. The length (head-feet direction) of the pad should be as long as the area of interest in that direction. The effect of changing the thickness of the pad is almost similar to changing the permittivity, e.g. by doubling the pad thickness and halving the permittivity you will get a similar B_1 distribution.

The placement of the pad should be as close to the body as possible and the center of the pad should be on top of the center of low signal intensity.

We have shown that the conductivity of the pad strongly influences the homogeneity of the B_1 field. In general we can conclude that the conductivity of the pads should be as low as possible.

From the permittivity optimization we can conclude that there are large measured improvements in homogeneity by using the pads when operating

the system in quadrature mode, which corresponds to the vast majority of single channel 3 T systems currently available in the world. Results from the statistical analyses showed that the coefficient went from 22% to 16%. These results were in most cases not possible by only using RF shimming.

Even when operating in dual transmit mode with RF shimming on a state-of-the-art multichannel system, the dielectric pads provided a statistically significant increase in image homogeneity.

It has been shown that the power necessary to make the T1 image decreases by applying the pads, in the quadrature and RF shimmed case, which translates to a reduction in the total power absorbed by the body.

After this study we can say now that by applying the optimized dielectric pads we can significantly increase the image quality of abdominal imaging at 3 T. These pads cost approximately one thousand dollars and can compete (and in several cases outperform) a dual transmit system of one million dollars. This study lays down the foundations of high permittivity material usage in improving MRI image quality and will probably trigger a number of follow-up research, which will greatly improve quality of MRI imaging in the future without significantly increasing the costs.

Bibliography

[1] M. A. Bernstein, r. Huston, John, and H. A. Ward, "Imaging artifacts at 3.0T," *Journal of magnetic resonance imaging: JMRI*, vol. 24, pp. 735–746, Oct. 2006. PMID: 16958057.

[2] D. Cornfeld and J. Weinreb, "Simple changes to 1.5-t MRI abdomen and pelvis protocols to optimize results at 3 t," *AJR. American journal of roentgenology*, vol. 190, pp. W140–150, Feb. 2008. PMID: 18212198.

[3] K. Chang and I. Kamel, "Abdominal imaging at 3t: challenges and solutions," *AJR. American journal of roentgenology*, vol. 39, pp. 21–31, Oct. 2010.

[4] O. Dietrich, M. F. Reiser, and S. O. Schoenberg, "Artifacts in 3-t MRI: physical background and reduction strategies," *European journal of radiology*, vol. 65, pp. 29–35, Jan. 2008. PMID: 18162353.

[5] R. K. Yang, C. G. Roth, R. J. Ward, J. O. deJesus, and D. G. Mitchell, "Optimizing abdominal MR imaging: approaches to common problems," *Radiographics: a review publication of the Radiological Society of North America, Inc*, vol. 30, pp. 185–199, Jan. 2010. PMID: 20083593.

[6] E. M. Merkle and B. M. Dale, "Abdominal MRI at 3.0 t: the basics revisited," *AJR. American journal of roentgenology*, vol. 186, pp. 1524–1532, June 2006. PMID: 16714640.

[7] M. Nelles, R. S. Knig, J. Gieseke, M. M. Guerand-van Battum, G. M. Kukuk, H. H. Schild, and W. A. Willinek, "Dual-source parallel RF transmission for clinical MR imaging of the spine at 3.0 t: intraindividual comparison with conventional single-source transmission," *Radiology*, vol. 257, pp. 743–753, Dec. 2010. PMID: 20858848.

[8] W. A. Willinek, J. Gieseke, G. M. Kukuk, M. Nelles, R. Knig, N. Morakkabati-Spitz, F. Trber, D. Thomas, C. K. Kuhl, and H. H. Schild, "Dual-source parallel radiofrequency excitation body MR imaging compared with standard MR imaging at 3.0 t: initial clinical experience," *Radiology*, vol. 256, pp. 966–975, Sept. 2010. PMID: 20720078.

[9] G. Adriany, P.-F. Van de Moortele, F. Wiesinger, S. Moeller, J. P. Strupp, P. Andersen, C. Snyder, X. Zhang, W. Chen, K. P. Pruessmann, P. Boesiger, T. Vaughan, and K. Uurbil, "Transmit and receive transmission line arrays for 7 tesla parallel imaging," *Magnetic resonance in medicine: official journal of the Society of Magnetic Resonance in Medicine / Society of Magnetic Resonance in Medicine*, vol. 53, pp. 434–445, Feb. 2005. PMID: 15678527.

[10] O. Kraff, A. K. Bitz, S. Kruszona, S. Orzada, L. C. Schaefer, J. M. Theysohn, S. Maderwald, M. E. Ladd, and H. H. Quick, "An eight-channel phased array RF coil for spine MR imaging at 7 t," *Investigative radiology*, vol. 44, pp. 734–740, Nov. 2009. PMID: 19809342.

[11] C. A. T. Van den Berg, B. van den Bergen, J. B. Van de Kamer, B. W. Raaymakers, H. Kroeze, L. W. Bartels, and J. J. W. Lagendijk, "Simultaneous b1 + homogenization and specific absorption rate hotspot suppression using a magnetic resonance phased array transmit coil," *Magnetic resonance in*

medicine: official journal of the Society of Magnetic Resonance in Medicine / Society of Magnetic Resonance in Medicine, vol. 57, pp. 577–586, Mar. 2007. PMID: 17326185.

[12] P. Vernickel, P. Rschmann, C. Findeklee, K.-M. Ldeke, C. Leussler, J. Overweg, U. Katscher, I. Grsslin, and K. Schnemann, "Eight-channel transmit/receive body MRI coil at 3T," *Magnetic resonance in medicine: official journal of the Society of Magnetic Resonance in Medicine / Society of Magnetic Resonance in Medicine*, vol. 58, pp. 381–389, Aug. 2007. PMID: 17654592.

[13] K. M. Franklin, B. M. Dale, and E. M. Merkle, "Improvement in b1-inhomogeneity artifacts in the abdomen at 3T MR imaging using a radiofrequency cushion," *Journal of magnetic resonance imaging: JMRI*, vol. 27, pp. 1443–1447, June 2008. PMID: 18421685.

[14] M. Sreenivas, M. Lowry, P. Gibbs, M. Pickles, and L. W. Turnbull, "A simple solution for reducing artefacts due to conductive and dielectric effects in clinical magnetic resonance imaging at 3T," *European journal of radiology*, vol. 62, pp. 143–146, Apr. 2007. PMID: 17169519.

[15] Y. Takayama, H. Nonaka, M. Nakajima, T. Obata, and H. Ikehira, "Reduction of a high-field dielectric artifact with homemade gel," *Magnetic resonance in medical sciences: MRMS: an official journal of Japan Society of Magnetic Resonance in Medicine*, vol. 7, no. 1, pp. 37–41, 2008. PMID: 18460847.

[16] M. Kataoka, H. Isoda, Y. Maetani, Y. Nakamoto, T. Koyama, S. Umeoka, K. Tamai, A. Kido, N. Morisawa, T. Saga, and K. Togashi, "MR imaging of the female pelvis at 3 tesla: evaluation of image homogeneity using different dielectric pads," *Journal of magnetic resonance imaging: JMRI*, vol. 26, pp. 1572–1577, Dec. 2007. PMID: 17968958.

[17] W. M. Teeuwisse, W. M. Brink, and A. G. Webb, "Quantitative assessment of the effects of high-permittivity pads in 7 tesla MRI of the brain," *Magnetic resonance in medicine: official journal of the Society of Magnetic Resonance in Medicine / Society of Magnetic Resonance in Medicine*, vol. 67, pp. 1285–1293, May 2012. PMID: 21826732.

[18] W. M. Teeuwisse, W. M. Brink, K. N. Haines, and A. G. Webb, "Simulations of high permittivity materials for 7 t neuroimaging and evaluation of a new barium titanate-based dielectric," *Magnetic resonance in medicine: official journal of the Society of Magnetic Resonance in Medicine / Society of Magnetic Resonance in Medicine*, vol. 67, pp. 912–918, Apr. 2012. PMID: 22287360.

[19] F. Bloch, "Nuclear induction," *Phys. Rev.*, vol. 70, pp. 460–474, Oct 1946.

[20] H. A. Lorentz, "The theorem of poynting concerning the energy in the electromagnetic field and two general propositions concerning the propagation of light," *Versl. Kon. Akad. Wentensch*, vol. 176, pp. 1–11, 1896.

[21] N. B. Smith and A. Webb, *Introduction to Medical Imaging: Physics, Engineering and Clinical Applications*. Cambridge University Press, 1 ed., Dec. 2010.

[22] T. Ibrahim, "Design of radiofrequency coild for magnetic resonance imaging applications: A computational electromagnetic approach," *Graduate school of the ohio state university*, 2003.

[23] J. G. Sled and G. B. Pike, "Standing-wave and RF penetration artifacts caused by elliptic geometry: an electrodynamic analysis of MRI," *IEEE transactions on medical imaging*, vol. 17, pp. 653–662, Aug. 1998. PMID: 9845320.

[24] T. B. A. Senior and J. L. Volakis, *Approximate Boundary Conditions in Electromagnetics*. Institution of Engineering and Technology, Mar. 1995.

[25] A. T. de Hoop and L. Jiang, "Pulsed EM field response of a thin, high-contrast, finely layered structure with dielectric and conductive properties," *IEEE Transactions on Antennas and Propagation*, vol. 57, pp. 2260 –2269, Aug. 2009.

[26] A. T. de Hoop, *Handbook of Radiation and Scattering of Waves*. Academic Press, Nov. 1995.

[27] A. Christ, W. Kainz, E. G. Hahn, K. Honegger, M. Zefferer, E. Neufeld, W. Rascher, R. Janka, W. Bautz, J. Chen, B. Kiefer, P. Schmitt, H.-P. Hollenbach, J. Shen, M. Oberle, D. Szczerba, A. Kam, J. W. Guag, and N. Kuster, "The virtual family–development of surface-based anatomical models of two adults and two children for dosimetric simulations," *Physics in medicine and biology*, vol. 55, pp. N23–38, Jan. 2010. PMID: 20019402.

[28] J. Wang, Q. X. Yang, X. Zhang, C. M. Collins, M. B. Smith, X.-H. Zhu, G. Adriany, K. Ugurbil, and W. Chen, "Polarization of the RF field in a human head at high field: A study with a quadrature surface coil at 7.0 t," *Magnetic Resonance in Medicine*, vol. 48, no. 2, p. 362369, 2002.

[29] V. L. Yarnykh, "Actual flip-angle imaging in the pulsed steady state: a method for rapid three-dimensional mapping of the transmitted radiofrequency field," *Magnetic resonance in medicine: official journal of the Society of Magnetic Resonance in Medicine / Society of Magnetic Resonance in Medicine*, vol. 57, pp. 192–200, Jan. 2007. PMID: 17191242.

[30] A. Webb, "Dielectric materials in magnetic resonance," *Concepts in Magnetic Resonance Part A*, vol. 38A, no. 4, p. 148184, 2011.

[31] Q. X. Yang, W. Mao, J. Wang, M. B. Smith, H. Lei, X. Zhang, K. Ugurbil, and W. Chen, "Manipulation of image intensity distribution at 7.0 t: passive RF shimming and focusing with dielectric materials," *Journal of magnetic resonance imaging: JMRI*, vol. 24, pp. 197–202, July 2006. PMID: 16755543.

[32] J. E. M. Snaar, W. M. Teeuwisse, M. J. Versluis, M. A. van Buchem, H. E. Kan, N. B. Smith, and A. G. Webb, "Improvements in high-field localized MRS of the medial temporal lobe in humans using new deformable high-dielectric materials," *NMR in biomedicine*, vol. 24, pp. 873–879, Aug. 2011. PMID: 21834010.

[33] Q. X. Yang, J. Wang, J. Wang, C. M. Collins, C. Wang, and M. B. Smith, "Reducing SAR and enhancing cerebral signal-to-noise ratio with high permittivity padding at 3 t," *Magnetic resonance in medicine: official journal of the Society of Magnetic Resonance in Medicine / Society of Magnetic Resonance in Medicine*, vol. 65, pp. 358–362, Feb. 2011. PMID: 21264928.

[34] J. T. Vaughan, C. J. Snyder, L. J. DelaBarre, P. J. Bolan, J. Tian, L. Bolinger, G. Adriany, P. Andersen, J. Strupp, and K. Ugurbil, "Whole-body imaging at 7T: preliminary results," *Magnetic resonance in medicine: official journal of the Society of Magnetic Resonance in Medicine / Society of Magnetic Resonance in Medicine*, vol. 61, pp. 244–248, Jan. 2009. PMID: 19097214.

[35] P. de Heer, W. M. Brink, B. J. Kooij, and A. G. Webb, "Increasing signal homogeneity and image quality in abdominal imaging at 3 t with very high permittivity materials," *Magnetic resonance in medicine: official journal of the Society of Magnetic Resonance in Medicine / Society of Magnetic Resonance in Medicine*, July 2012. PMID: 22851426.

[36] T. S. Ibrahim, "Analytical approach to the MR signal," *Magnetic Resonance in Medicine*, vol. 54, no. 3, pp. 677–682, 2005.